ANALYSIS, DESIGN, AND CONTROL OF A NOVEL HALBACH-ARRAY-BASED TWO-PHASE MOTOR

A Thesis

by

YUAN WEI

Submitted to the Office of Graduate and Professional Studies of
Texas A&M University
in partial fulfillment of the requirements for the degree of

MASTER OF SCIENCE

Chair of Committee,   Won-jong Kim
Committee Members,   Mehrdad Ehsani
                       Pilwon Hur
Head of Department,   Andreas Polycarpou

December 2020

Major Subject: Mechanical Engineering

ABSTRACT

This thesis presents a new Halbach-array-based two-phase motor. The motor is based on a 2-pole, 10-segment Halbach cylinder that generates a uniform magnetic field inside. This uniform field simplifies the torque calculation and gives the basis of position detection based on Hall-effect sensors. This thesis gives a general analytical method to find the magnetic field intensity inside the Halbach cylinder. The analytical field solution is verified by a finite-element analysis (FEA) and experimental results from Hall-effect sensors. The two-phase armature can generate constant torque in the uniform magnetic field. With a transconductance amplifier, the maximum torque and speed generated by the motor with the current input of 4 A are 0.057 N·m and 276 rpm, respectively. With the controller developed in the thesis, this motor offers a self-position sensing method by two-phase Hall-effect sensors connecting to an Arduino microcontroller with a 0.5° resolution. The motor has the capacity to track the commanded motion and speed with error less than 0.6°.

ACKNOWLEDGEMENTS

I would like to thank my committee chair, Dr. Won-jong Kim, who is also my research advisor. During the time spent with him, he has been more like a mentor to me. I respect so much his academic achievements in the electromagnetism, control theory, and mechatronics field. I really learnt a lot. I also want to thank my committee members, Dr. Mehrdad Ehsani and Dr. Pilwon Hur. Without their continuous understanding and valuable help, I could not go this far.

I appreciate the technical help from Dr. Vu Nguyen. His advice was very useful and helpful to improve my research. I also want to thank Dr. Guy Battle, who gave me hints to solve the partial differential equation in the thesis.

Thanks also go to Ivan Cortes and Robert Lipham in the Precision Mechatronics Lab, who taught me a lot when I first came to Texas A&M University. I also want to thank to Wei Lu in the University of Tokyo. They gave me lots of technical advice to solve the problem during the research.

I couldn't thank my parents, Wei Wei and Haiyan Zhou, enough for their encouragement and financial support to finish my Master of Science degree. They are always my strongest support.

Finally, thanks to Zilin Cai, Wenjie Weng, Tianxing Wang, Lida Shen, and Qian Cao. They are my best friends. We supported each every other during this epidemic outbreak around the world in 2020.

NOMENCLATURE

$\boldsymbol{A}$	magnetic vector potential (T·m)
ABS	acrylonitrile butadiene styrene
ADC	analog-to-digital converter
AWG	American wire gauge
$\boldsymbol{B}$	magnetic flux density (T)
$\boldsymbol{B}_{rem}$	remanence (T)
C	capacitance (F)
DAC	digital-to-analog converter
FEA	finite-element analysis
HABTPM	Halbach-array-based two-phase motor
i	current (A)
$\boldsymbol{J}$	current density (A/m^2)
J_m	moment of inertia of the motor (kg· m^2)
L	inductance (H)
$\boldsymbol{M}$	magnetization (A/m)
PI	proportional–integral
PM	permanent magnet
R	resistance (Ω)
r	radius (m)
T	temperature (°C)

t	time (s)
V	voltage (V)
V_{cc}	power supply voltage(V)
ζ	damping ratio
θ	angle in the cylindrical coordinate of Halbach cylinder (rad)
μ	permeability (H/m)
μ_0	permeability of free space: $4\pi \times 10^{-7}$ H/m
τ	torque (N·m)
ϕ	magnetic flux (Wb)
ψ	angular of the motor (rad)
$\dot{\psi}$	angular velocity of the motor (rad/s)
$\ddot{\psi}$	angular acceleration of the motor (rad/s^2)
ω_n	natural frequency (rad/s)

TABLE OF CONTENTS

Page

LIST OF FIGURES

ix

LIST OF TABLES

1. INTRODUCTION

A Halbach magnet array is a special placement of permanent magnets that generates a strong magnetic field on one side of the array but weak on the other side [1]. The single-sided field gives an advantage of concentrating the magnetic energy. A Halbach array also generates a sinusoidal wave of magnetic flux density in space, which gives an advantage to track the position with Hall-effect sensors. This effect is widely applied in the planar position control [2]–[4]. The cylindrical Halbach magnet array, which is also described as Halbach cylinder, can be used in motor design [5]–[6].

1.1. Halbach Array

Normally, magnets of a planar Halbach array are placed at 90° rotation. As shown in Figure 1.1, if magnets are placed in clockwise rotation from the left to the right, the magnetic field on the bottom side of the array is stronger, and the fundamental magnetic field on the top side is zero. The magnetic flux density of the Halbach array placement is larger that of conventional placements as shown in Figure 1.1.

The magnetic flux density changes sinusoidally along the axis parallel to the array on the strong side of the Halbach array with constant distance [7]–[8]. Although this effect is based on the assumption of an infinite length of magnet array, it can be applied to planar magnetic levitation and moving control. For example, Trumper *et al.* have presented the design paradigm and theory based on this effect [7]. If the Halbach array is put in a hollow, cylindrical structure instead of a planar, it can concentrate the magnetic field inside the

cylinder and, with two-pole case, will generate a uniform magnetic flux density as well as shown in Section 2.1.2.
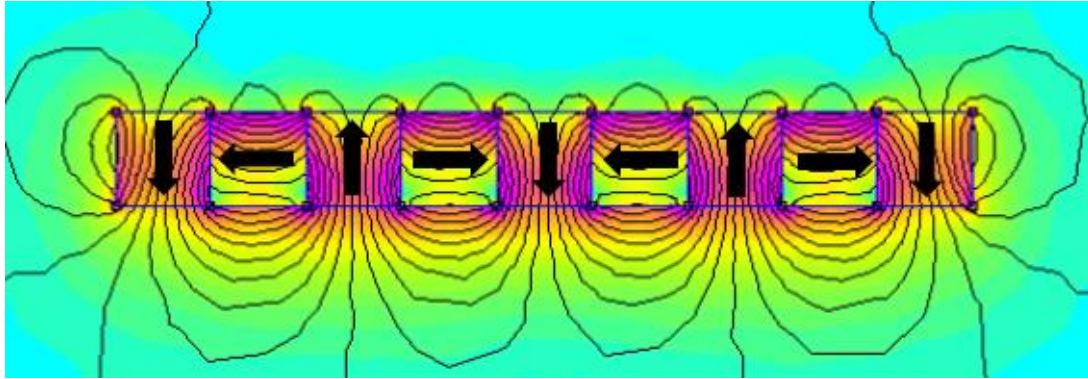
(a)
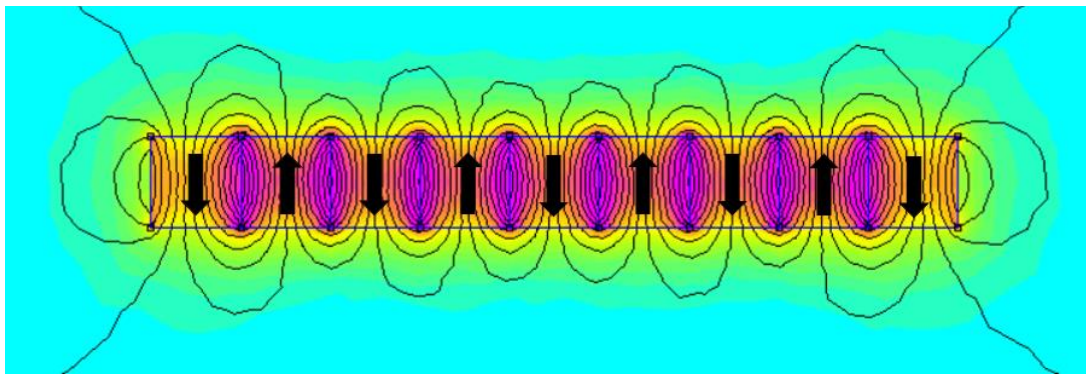
(b)

Figure 1.1 (a) Linear Halbach magnet array with the 90° magnetization rotation and (b) conventional magnet array.

1.2. Halbach Cylinder

There are two types of the Halbach cylinder–The one with an internal field and the other with an external field to work with an internal rotor or external armature. Since this

research focuses on a design of a permanent-magnet (PM) motor with an internal armature, a Halbach cylinder with an internal field is illustrated in detail.

In the ideal Halbach cylinder with an internal field, a sinusoidally varying magnetization is required. If the magnets have the placement of one period around the cylinder, namely a 2-pole structure, an ideal uniform magnetic field distribution is present at the center of the cylinder. Insinga *et al.* gave the Halbach equation as [9]

$$B = B_{rem} \ln \left(\frac{R_o}{R_i} \right) \tag{1.1}$$

where B is the magnetic flux density in the air gap, B_{rem} is the residual magnetic flux density of the magnet, R_o and R_i are the outer and inner radii of the cylinder. In reality, however, this ideal Halbach cylinder is infeasible to fabricate. One way to approximate the Halbach cylinder is to fill the cylinder with segmented magnets. Figure 1.2 shows the finite-element analysis (FEA) image of the flux lines.
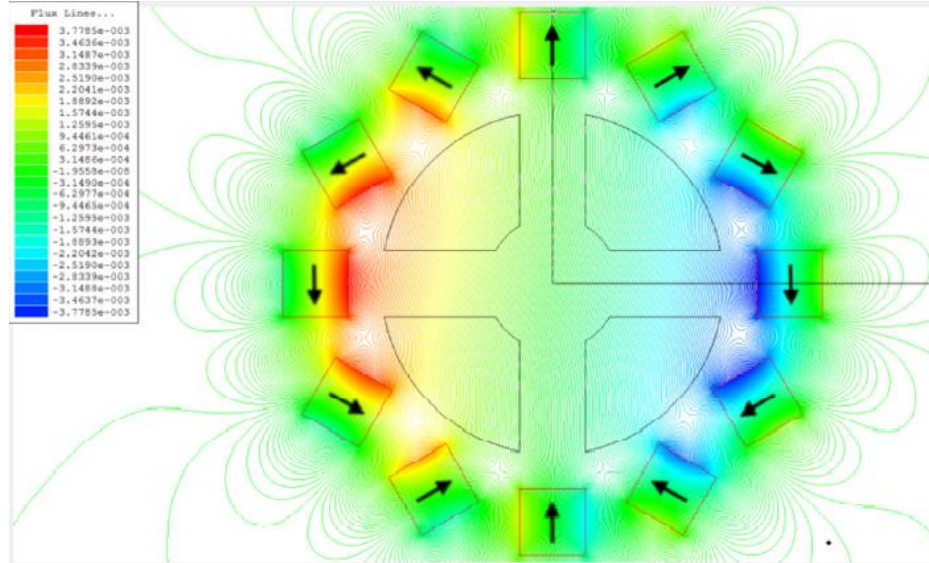
Figure 1.2 The FEA image of the 2-pole, 6-segment Halbach cylinder.

In the air gap, this structure gives a practical means to create a sinusoidal flux-density distribution for the application in high-precision positioning. The analysis of predicting the field distribution of a segmented Halbach cylinder was given by Shi *et al.* [10]. However, in the case discussed in the paper, there is no air gap between magnets. In real design, it is impossible to place an armature or magnets without an air gap inside a cylindrical geometry. Chen *et al.* provided a limited-angle torque motor with a single-phase rotor based on a segmented Halbach cylinder and managed to establish the angular position control system [6], but it has limitations of non-constant torque production in a full period and low motor speed, and their four-segment structure could not generate a fine, uniform magnetic flux density.

1.3. Contributions of this Research

This research constructed a system as shown in the Figure 1.3, the overall system of this HABTPM consists of Arduino for data collecting and controller, DAC and ADC to output and input data, voltage shifter, current amplifier to generate various current to the motor, and HABTM. The proposed research is to develop a new Halbach-array-based two-phase motor (HABTPM), which includes (1) designing and developing a Halbach cylinder that can generate uniform magnet field density inside, (2) establishing an analytical framework for the general Halbach-array-based two-phase motor that can produce constant torque, (3) proposing a high-precision position sensing method based on Hall-effect sensors, and (4) designing and implementing a controller to achieve precision position control.

14
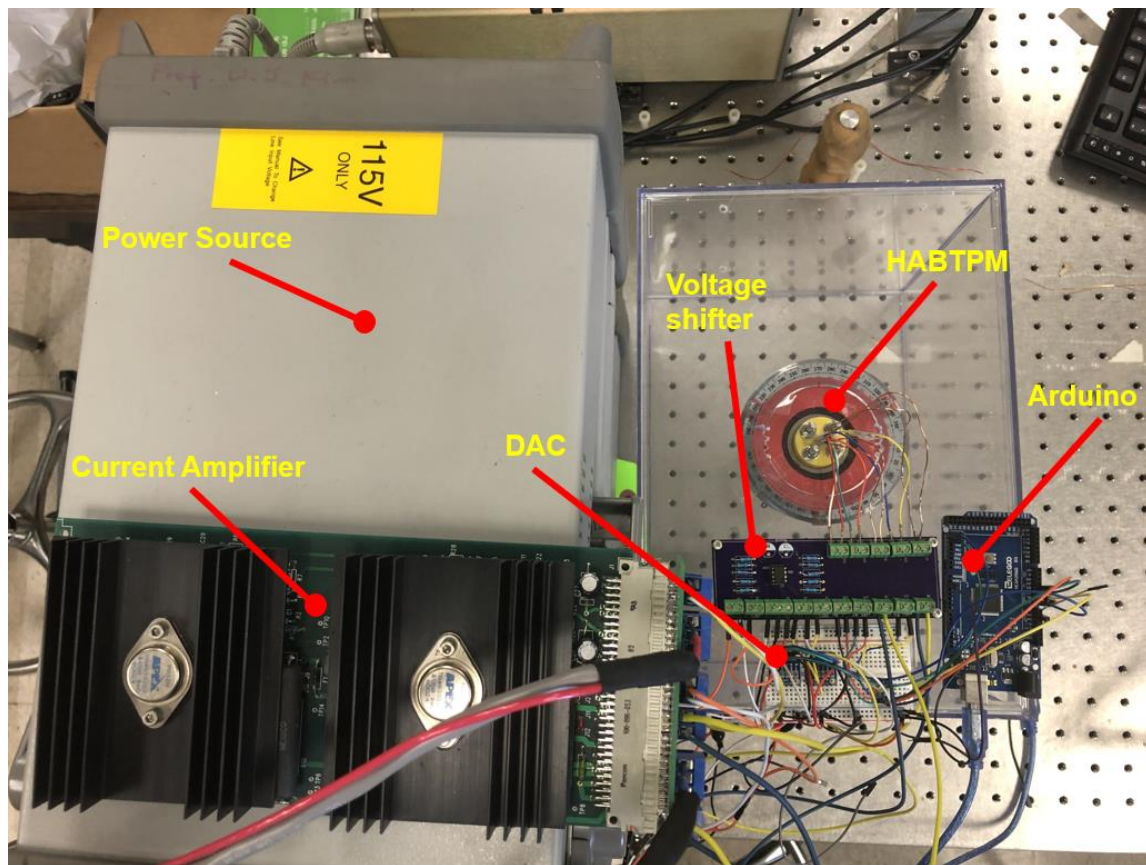
Figure 1.3 The overall system of the HABTPM

2. ELECTROMAGNETIC ANALYSIS

As shown in Figure 2.1, magnets are placed in the outer cylinder that generates strong internal magnetic field and the stator with coils that carry current is placed in the inner cylinder. This model is for general PM motor that has inner stator with armatures [11].
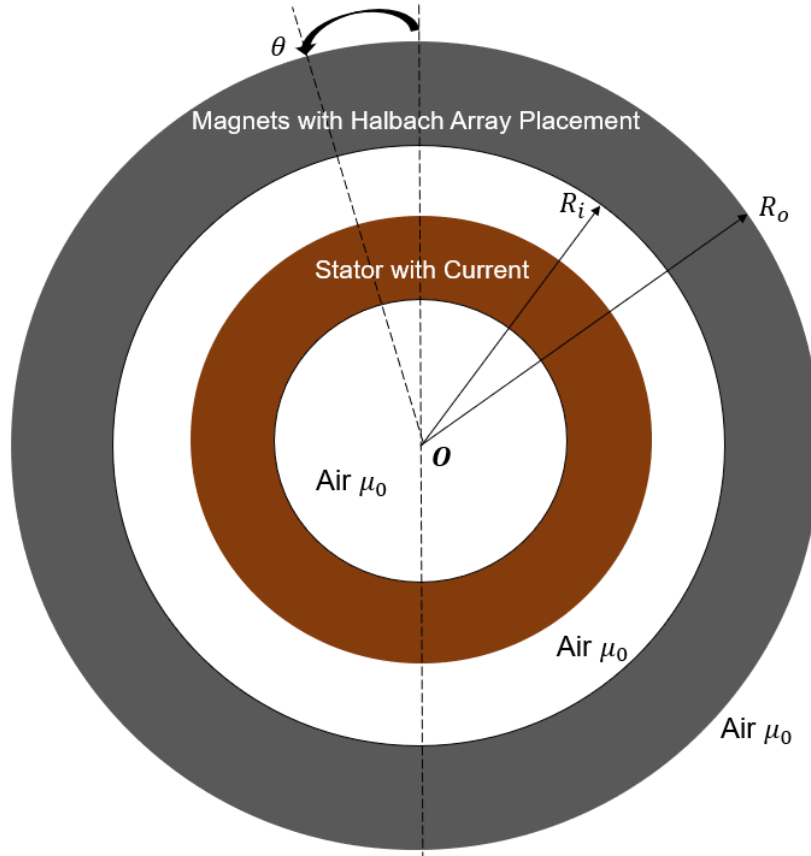
Figure 2.1 The model of HABTPM.

In this chapter, the theoretical analysis of a general Halbach cylinder based on the magnetoquasistatic (MQS) approximation is presented. After the general expression of the magnetic flux density is derived, a segmented design is considered. The HABTPM

employs a 2-pole, 10-segment Halbach cylinder. Because of the air gap between the magnets, this magnet cylinder generates a different set of the Fourier harmonics in the magnetic flux density. The magnetic flux density inside the cylinder in the Fourier series is then compared with the finite-element analysis (FEA) result.

2.1. Magnetic Field Analysis of Halbach Cylinder

2.1.1. Poisson's Equation for Vector Potential

Under the MQS approximation [17], the effect of the time-varying electric field is neglected. The Halbach magnet cylinder has no current source, so the free volume and surface current densities $\boldsymbol{J}_f$ and $\boldsymbol{K}_f$ are not present. Then, the governing equations are

$$\nabla \cdot \boldsymbol{B} = 0 \tag{2.1}$$

$$\nabla \times \boldsymbol{H} = \boldsymbol{J}_f = 0 \tag{2.2}$$

$$\boldsymbol{B} = \mu_0(\boldsymbol{H} + \boldsymbol{M}) \tag{2.3}$$

$$\nabla \times \boldsymbol{E} = -\frac{\partial \boldsymbol{B}}{\partial t} \tag{2.4}$$

$$\nabla \cdot \boldsymbol{J}_f = 0 \tag{2.5}$$

We assume the magnetically linear medium

$$\boldsymbol{B} = \mu\boldsymbol{H} = \mu_0\boldsymbol{H} \tag{2.6}$$

The boundary condition is

$$\boldsymbol{n} \times (\boldsymbol{B}^a - \boldsymbol{B}^b) = \mu_0\boldsymbol{K}_f + \mu_0\boldsymbol{n} \times (\boldsymbol{M}^a - \boldsymbol{M}^b) = \mu_0\boldsymbol{n} \times (\boldsymbol{M}^a - \boldsymbol{M}^b) \tag{2.7}$$

where μ_0 is the permeability of free space, $4\pi \times 10^{-7}$ H/m. The magnetic vector potential $\boldsymbol{A}$ is defined as

$$\boldsymbol{B} \equiv \nabla \times \boldsymbol{A} \qquad (2.8)$$

Taking the curl for (2.8), we get

$$\nabla \times \boldsymbol{B} = \nabla \times (\nabla \times \boldsymbol{A}) = \nabla(\nabla \cdot \boldsymbol{A}) - \nabla^2 \boldsymbol{A} \qquad (2.9)$$

by a vector identity. Setting the Coulomb gauge, $\nabla \cdot \boldsymbol{A} = 0$, and substituting (2.2) and (2.3) into (2.8) yields the following Poisson's equation.

$$\nabla^2 \boldsymbol{A} = -\mu_0 \nabla \times \boldsymbol{M} \qquad (2.10)$$

2.1.2. General Solution to the General Poisson's Equation

The Halbach cylinder model is shown in Figure 2.2, with the inner radius of R_i and the outer radius R_o. On the outer surface, there are boundary a and b. On the inner surface, there are boundary c and d. The magnetization $\boldsymbol{M}$ is that of the Halbach cylinder. The system is established in the cylindrical coordinates.

In the cylindrical coordinates, the magnetization density $\boldsymbol{M}$ of any periodic magnet placement in the cylinder can be expressed as a Fourier series.

$$\boldsymbol{M} = M_r \boldsymbol{i}_r + M_\theta \boldsymbol{i}_\theta = \sum_{n=1}^{\infty} M_{rn} \cos(n\theta) \, \boldsymbol{i}_r + M_{\theta n} \sin(n\theta) \boldsymbol{i}_\theta \qquad (2.11)$$

where M_{rn} and $M_{\theta n}$ are nth Fourier harmonics of its r- and θ-components, respectively. The cylinder generates the strong internal field when $M_{rn} = M_{\theta n}$ and the strong external field when $M_{rn} = -M_{\theta n}$ [11]. Substituting (2.11) into (2.10) in the volume of the magnets, the vector Poisson equation for the nth harmonics becomes

$$\nabla^2 \boldsymbol{A}_n = -\frac{\mu_0}{r} (M_{rn} + n M_{\theta n}) \sin(n\theta) \boldsymbol{i}_z \qquad (2.12)$$
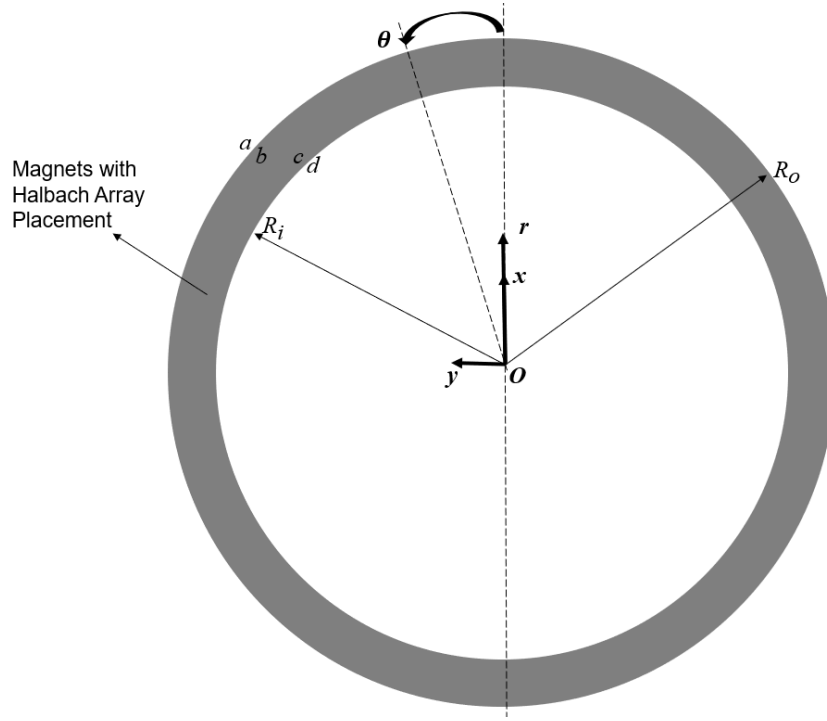
Figure 2.2 General Halbach cylinder model with boundary condition.

The magnetization is in the r-θ plane, so the vector potential has only z-component. From (2.12), with the separation of variables, $\boldsymbol{A}_n$ can be written as

$$\boldsymbol{A}_n = A_{zn}(r)\sin(n\theta)\,\boldsymbol{i}_z \tag{2.13}$$

Equation (2.12) becomes a Cauchy-Euler equation in the cylindrical coordinate system as

$$\frac{\partial^2 A_{zn}}{\partial r^2} + \frac{1}{r}\cdot\frac{\partial A_{zn}}{\partial r} - \frac{n^2}{r^2}A_{zn} = -\frac{\mu_0}{r}(M_{rn} + nM_{\theta n}) \tag{2.14}$$

The homogeneous solution is given in (2.15).

$$A_{znh}(r) = C_{n1}r^n + C_{n2}r^{-n} \tag{2.15}$$

The particular solution is shown in (2.16)–(2.17).

$$A_{z1p}(r) = -\frac{\mu_0(M_{r1}+M_{\theta 1})}{2}r\ln(r), n = 1 \tag{2.16}$$

$$A_{znp}(r) = \frac{r\mu_0(M_{rn}+nM_{\theta n})}{n^2-1}, \quad n \neq 1 \tag{2.17}$$

C_{n1} and C_{n2} are the constants to be determined by the boundary conditions. The solution to (2.14) is

$$A_{z1}(r) = C_{11}r + C_{12}r^{-1} - \frac{\mu_0(M_{r1}+M_{\theta 1})}{2}r\ln(r), \quad n = 1 \tag{2.18}$$

$$A_{zn}(r) = C_{n1}r^n + C_{n2}r^{-n} + \frac{r\mu_0(M_{rn}+nM_{\theta n})}{n^2-1}, \quad n \neq 1 \tag{2.19}$$

We apply the boundary condition into A shown in (2.20) and (2.21), then get

$$\boldsymbol{A}_n(R_i) = A_{zn}(R_i)\sin(n\theta)\boldsymbol{i_z} = A_{zn}^c\sin(n\theta)\boldsymbol{i_z} \tag{2.20}$$

$$\boldsymbol{A}_n(R_o) = A_{zn}(R_o)\sin(n\theta)\boldsymbol{i_z} = A_{zn}^b\sin(n\theta)\boldsymbol{i_z} \tag{2.21}$$

where A_{zn}^c and A_{zn}^b are the z-component of the nth harmonic of magnetic vector potential $\boldsymbol{A}_n$ evaluated at $r = R_i$ and R_o, respectively.

The transfer relations between the magnetic flux density and the magnetic vector potential can be derived by solving (2.18)–(2.21) [17]. Following Sections 2.1.3 and 2.1.4 illustrate the field solution based on the transfer relations in the fundamental and nth spatial harmonics, respectively.

2.1.3. Field Solution for the Fundamental Fourier Harmonics

We treat the case of $n = 1$ first. If it is a Halbach cylinder with internal field, $M_{r1} = M_{\theta 1}$. The constants C_{11} and C_{12} are found by applying (2.20) and (2.21) into (2.18). Then we have the solution of $A_{z1}(r)$.

$$C_{11} = \frac{1}{R_o^2-R_i^2}\left\{A_{z1}^b R_o - A_{z1}^c R_i + \frac{\mu_0(M_{r1}+M_{\theta 1})}{2}[R_o^2\ln(R_o) - R_i^2\ln(R_i)]\right\} \tag{2.22}$$

20

$$C_{12} = A_{z1}^c R_i + \frac{\mu_0(M_{r1}+M_{\theta1})R_i^2 \ln(R_i)}{2} - \frac{R_i^2}{R_o^2-R_i^2}\left\{A_{z1}^b R_o - A_{z1}^c R_i + \frac{\mu_0(M_{r1}+M_{\theta1})}{2}[R_o^2 \ln(R_o) - \right.$$

$$\left. R_i^2 \ln(R_i)]\right\} \tag{2.23}$$

Evaluate (2.8) in the cylindrical coordinate system, we have

$$\boldsymbol{B} = \nabla \times \boldsymbol{A} = \frac{1}{r}\begin{vmatrix} \boldsymbol{i}_r & r\boldsymbol{i}_\theta & \boldsymbol{i}_z \\ \frac{\partial}{\partial r} & \frac{\partial}{\partial \theta} & 0 \\ 0 & 0 & A_{z1}\sin(\theta) \end{vmatrix} = \frac{1}{r}A_{z1}\cos(\theta)\,\boldsymbol{i}_r - \frac{\partial A_{z1}}{\partial r}\sin(\theta)\,\boldsymbol{i}_\theta \tag{2.24}$$

Take $\boldsymbol{B}_1 = B_{r1}\cos(\theta)\boldsymbol{i}_r + B_{\theta1}\sin(\theta)\boldsymbol{i}_\theta$, so $B_{\theta1} = -\frac{\partial A_{z1}}{\partial r}$. At $r = R_i$ and R_o, the

transfer relations between $B_{\theta1}$ and A_{z1} at the boundaries b and c become

$$\begin{bmatrix} B_{\theta1}^b \\ B_{\theta1}^c \end{bmatrix} = \begin{bmatrix} \frac{R_i^2+R_o^2}{R_o(R_i^2-R_o^2)} & \frac{2R_i}{R_o^2-R_o^2} \\ \frac{2R_o}{R_i^2-R_o^2} & \frac{R_i^2+R_o^2}{R_i(R_o^2-R_i^2)} \end{bmatrix}\begin{bmatrix} A_{z1}^b \\ A_{z1}^c \end{bmatrix} + \begin{bmatrix} 1 + \frac{2R_i^2[\ln(R_i)-\ln(R_o)]}{R_o^2-R_i^2} \\ 1 + \frac{2R_o^2[\ln(R_i)-\ln(R_o)]}{R_o^2-R_i^2} \end{bmatrix}\frac{\mu_0(M_{r1}+M_{\theta1})}{2} \tag{2.25}$$

Inside the volume of the magnets in (2.25), the right-hand side contains the

homogeneous and the source terms. The homogeneous term is a general form of transfer

relations between magnetic flux density and the magnetic vector potential in free space

[17]. The free space for $r > R_o$ and $r < R_i$ contains no source term, so (2.14) is rewritten

into (2.26) in this space.

$$\frac{\partial^2 A_{z1}}{\partial r^2} + \frac{1}{r}\cdot\frac{\partial A_{z1}}{\partial r} - \frac{1}{r^2}A_{z1} = 0 \tag{2.26}$$

which is a homogeneous Cauchy-Euler equation. In the free space with the arbitrary radius

α and β, where $\alpha > \beta$, the transfer relations between the magnetic flux density and the

magnetic vector potential is given as (2.27) [17].

$$\begin{bmatrix} B_{\theta1}^\alpha \\ B_{\theta1}^\beta \end{bmatrix} = \begin{bmatrix} \frac{\alpha^2+\beta^2}{\alpha(\beta^2-\alpha^2)} & \frac{2\beta}{\alpha^2-\beta^2} \\ \frac{2\alpha}{\beta^2-\alpha^2} & \frac{\alpha^2+\beta^2}{\beta(\alpha^2-\beta^2)} \end{bmatrix}\begin{bmatrix} A_{z1}^\alpha \\ A_{z1}^\beta \end{bmatrix} \tag{2.27}$$

For the free space for $r > R_o$, $\alpha \to \infty$ and $\beta = R_o$. Hence,

$$B_{\theta 1}^a = \frac{1}{R_o} A_{z1}^a \tag{2.28}$$

Take the same procedure for the free space for $r < R_i$ with $\alpha = R_i$ and $\beta \to 0$. Hence,

$$B_{\theta 1}^d = -\frac{1}{R_i} A_{z1}^d \tag{2.29}$$

Next step is to find the jump in the magnetic flux density at the boundary. Applying (2.7) on outer surface and inner surface, we get the boundary conditions (2.30)–(2.31).

$$-B_{\theta 1}^a + B_{\theta 1}^b = \mu_0 M_{\theta 1} = \frac{\mu_0 (M_{r1} + M_{\theta 1})}{2} \tag{2.30}$$

$$-B_{\theta 1}^c + B_{\theta 1}^d = -\mu_0 M_{\theta 1} = -\frac{\mu_0 (M_{r1} + M_{\theta 1})}{2} \tag{2.31}$$

The vector potential is continuous at any boundaries, so

$$A_{z1}^a = A_{z1}^b \tag{2.32}$$

$$A_{z1}^c = A_{z1}^d \tag{2.33}$$

Now there are 4 equations (2.25), (2.28), and (2.29) of transfer relations, 4 boundary conditions (2.30)–(2.33). Putting those 8 equations in matrix from with 8 variables

$$\begin{bmatrix} 1 & -1 & 0 & 0 & 0 & 0 & 0 & 0 \\ 0 & 0 & 1 & -1 & 0 & 0 & 0 & 0 \\ \frac{1}{R_o} & 0 & 0 & 0 & -1 & 0 & 0 & 0 \\ 0 & -F_1 & -G_1 & 0 & 0 & 1 & 0 & 0 \\ 0 & -G_2 & -F_2 & 0 & 0 & 0 & 1 & 0 \\ 0 & 0 & 0 & \frac{1}{R_i} & 0 & 0 & 0 & 1 \\ 0 & 0 & 0 & 0 & -1 & 1 & 0 & 0 \\ 0 & 0 & 0 & 0 & 0 & 0 & -1 & 1 \end{bmatrix} \begin{bmatrix} A_{z1}^a \\ A_{z1}^b \\ A_{z1}^c \\ A_{z1}^d \\ B_{\theta 1}^a \\ B_{\theta 1}^b \\ B_{\theta 1}^c \\ B_{\theta 1}^d \end{bmatrix} = \begin{bmatrix} 0 \\ 0 \\ 0 \\ 0 \\ T_1 \\ T_2 \\ 0 \\ 1 \\ -1 \end{bmatrix} \frac{\mu_0 (M_{r1} + M_{\theta 1})}{2} \tag{2.34}$$

where

$$F_1 = \frac{R_i^2 + R_o^2}{R_o(R_i^2 - R_o^2)} \tag{2.35}$$

$$F_2 = \frac{R_i^2 + R_o^2}{R_i(R_o^2 - R_i^2)} \tag{2.36}$$

$$G_1 = \frac{2R_i}{R_o^2 - R_o^2} \tag{2.37}$$

$$G_2 = \frac{2R_o}{R_i^2 - R_o^2} \tag{2.38}$$

$$T_1 = 1 + \frac{2R_i^2[\ln(R_i) - \ln(R_o)]}{R_o^2 - R_i^2} \tag{2.39}$$

$$T_2 = 1 + \frac{2R_o^2[\ln(R_i) - \ln(R_o)]}{R_o^2 - R_i^2} \tag{2.40}$$

Solving for (2.34),

$$\begin{bmatrix} A_{z1}^a \\ A_{z1}^b \\ A_{z1}^c \\ A_{z1}^d \\ B_{\theta 1}^a \\ B_{\theta 1}^b \\ B_{\theta 1}^c \\ B_{\theta 1}^d \end{bmatrix} = \begin{bmatrix} 0 \\ 0 \\ \frac{\mu_0(M_{r1} + M_{\theta 1})}{2} R_i \ln\left(\frac{R_o}{R_i}\right) \\ \frac{\mu_0(M_{r1} + M_{\theta 1})}{2} R_i \ln\left(\frac{R_o}{R_i}\right) \\ 0 \\ \frac{\mu_0 M_1}{2} \\ \frac{\mu_0(M_{r1} + M_{\theta 1})}{2}[1 - \ln\left(\frac{R_o}{R_i}\right)] \\ -\frac{\mu_0(M_{r1} + M_{\theta 1})}{2}\ln\left(\frac{R_o}{R_i}\right) \end{bmatrix} \tag{2.41}$$

From (2.41), we have

$$B_{\theta 1}^d = -\frac{\mu_0(M_{r1} + M_{\theta 1})}{2}\ln\left(\frac{R_o}{R_i}\right) \tag{2.42}$$

Because $M_{r1} + M_{\theta 1} = 2M_{\theta 1} = 2M_{r1} = 2 \cdot \frac{B_{rem}}{\mu_0}$ in an ideal 2-pole Halbach

cylinder with internal field, B_θ^d becomes

$$B_{\theta 1}^d = -B_{rem}\ln\left(\frac{R_o}{R_i}\right) \tag{2.43}$$

23

At any arbitrary position (r_0, θ_0), where $0 < r_0 < R_i$ and $0 \le \theta \le 2\pi$. It is the same condition as (2.29), so we have

$$B_\theta^{r_0} = -\frac{1}{r_0} A_z^{r_0} \tag{2.44}$$

Take $\alpha = R_i$ and $\beta = r_0$ in (2.27). The transfer relations are

$$\begin{bmatrix} B_{\theta 1}^d \\ B_{\theta 1}^{r_0} \end{bmatrix} = \begin{bmatrix} \frac{R_i^2 + r_0^2}{R_i(r_0^2 - R_i^2)} & \frac{2r_0}{R_i^2 - r_0^2} \\ \frac{2R_i}{r_0^2 - R_i^2} & \frac{R_i^2 + r_0^2}{r_0(R_i^2 - r_0^2)} \end{bmatrix} \begin{bmatrix} A_{z1}^d \\ A_{z1}^{r_0} \end{bmatrix} \tag{2.45}$$

Combining (2.41), (2,44), and (2.45),

$$B_{\theta 1}^{r_0} = B_{\theta 1}^d = -\frac{\mu_0 (M_{r1} + M_{\theta 1})}{2} \ln\left(\frac{R_o}{R_i}\right) \tag{2.46}$$

$$A_{z1}^{r_0} = \frac{r_0}{R_i} A_{z1}^d = r_0 \frac{\mu_0 (M_{r1} + M_{\theta 1})}{2} \ln\left(\frac{R_o}{R_i}\right) \tag{2.47}$$

From (2.24), $B_r^{r_0}$ is

$$B_{r1}^{r_0} = \frac{1}{r_0} A_{z1}^{r_0} = \frac{\mu_0 (M_{r1} + M_{\theta 1})}{2} \ln\left(\frac{R_o}{R_i}\right) \tag{2.48}$$

Comparing (2.46) and (2.48), we conclude that $B_{\theta 1}^{r_0} = -B_{r1}^{r_0}$. Because $\boldsymbol{B}_1 = B_{r1}\cos(\theta)\boldsymbol{i}_r + B_{\theta 1}\sin(\theta)\boldsymbol{i}_\theta$, the magnetic flux density at an arbitrary position (r_0, θ_0) inside the cylinder is

$$\boldsymbol{B}_1^{r_0} = \mu_0 M_{r1} \ln\left(\frac{R_o}{R_i}\right) [\cos(\theta_0)\boldsymbol{i}_r - \sin(\theta_0)\boldsymbol{i}_\theta] = \mu_0 M_{r1} \ln\left(\frac{R_o}{R_i}\right) \boldsymbol{i}_x \tag{2.49}$$

This equation indicates that the fundamental component of magnetic flux density generated by an ideal 2-pole Halbach cylinder with internal field is uniform anywhere inside the cylinder. Because $M_{r_1} = \frac{B_{rem}}{\mu_0}$ in an ideal 2-pole Halbach cylinder with internal

24

field, $\boldsymbol{B}_1^{r_0} = B_{rem} \ln\left(\frac{R_o}{R_i}\right) \boldsymbol{i}_x$. The result is consistent with the equation given by Insinga *et al.* [9].

2.1.4. Field Solution for the *N*th Fourier Harmonics

Substituting (2.20)–(2.21) into (2.19), the constants C_{n1} and C_{n2} are

$$C_{n1} = \frac{1}{R_o^n - R_i^{2n} R_o^{-n}} \left[A_{zn}^b - A_{zn}^c R_i^n R_o^{-n} - \frac{\mu_0(M_{rn} + nM_{\theta n})}{n^2 - 1}\left(R_o - R_i^{n+1} R_o^{-n}\right)\right] \quad (2.50)$$

$$C_{n2} = -\frac{R_i^{2n}}{R_o^n - R_i^{2n} R_o^{-n}} \left[A_{zn}^b - A_{zn}^c R_i^n R_o^{-n} - \frac{\mu_0(M_{rn} + nM_{\theta n})}{n^2 - 1}\left(R_o - R_i^{n+1} R_o^{-n}\right) + A_{zn}^c R_i^n - \right.$$

$$\frac{\mu_0(M_{rn} + nM_{\theta n})R_i^{n+1}}{n^2 - 1} \quad (2.51)$$

From $\boldsymbol{B} = \nabla \times \boldsymbol{A}$ as in (2.24), (2.25) is rewritten as

$$\begin{bmatrix} B_{\theta n}^b \\ B_{\theta n}^c \end{bmatrix} = \begin{bmatrix} \frac{n(R_i^{2n} + R_o^{2n})}{R_o(R_i^{2n} - R_o^{2n})} & \frac{2nR_i^n R_o^n}{R_o(R_o^{2n} - R_o^{2n})} \\ \frac{2nR_o^n R_i^n}{R_i(R_i^{2n} - R_o^{2n})} & \frac{n(R_i^{2n} + R_o^{2n})}{R_i(R_o^{2n} - R_i^{2n})} \end{bmatrix} \begin{bmatrix} A_{zn}^b \\ A_{zn}^c \end{bmatrix} + \begin{bmatrix} -\frac{1}{n^2 - 1} + \frac{n(R_o^{2n} + R_i^{2n} - 2R_o^{n-1} R_i^{n+1})}{(n^2 - 1)(R_o^{2n} - R_i^{2n})} \\ -\frac{1}{n^2 - 1} + \frac{n(R_o^{2n} + R_i^{2n} - 2R_i^{n-1} R_o^{n+1})}{(n^2 - 1)(R_o^{2n} - R_i^{2n})} \end{bmatrix} \mu_0(M_{rn} + $$

$$nM_{\theta n}) \quad (2.52)$$

The homogeneous solution for the *n*th harmonics is rewritten as (2.53) [17].

$$\begin{bmatrix} B_{\theta n}^\alpha \\ B_{\theta n}^\beta \end{bmatrix} = \begin{bmatrix} \frac{n(\alpha^{2n} + \beta^{2n})}{\alpha(\beta^{2n} - \alpha^{2n})} & \frac{2n\alpha^n \beta^n}{\alpha(\alpha^{2n} - \beta^{2n})} \\ \frac{2n\alpha^n \beta^n}{\beta(\beta^{2n} - \alpha^{2n})} & \frac{n(\alpha^{2n} + \beta^{2n})}{\beta(\alpha^{2n} - \beta^{2n})} \end{bmatrix} \begin{bmatrix} A_{zn}^\alpha \\ A_{zn}^\beta \end{bmatrix} \quad (2.53)$$

For the free space for $r > R_o$ and $r < R_i$,

$$B_{\theta n}^a = \frac{n}{R_o} A_{zn}^a \quad (2.54)$$

$$B_{\theta n}^d = -\frac{n}{R_i} A_{zn}^d \quad (2.55)$$

The boundary conditions for the magnetic flux density are

25

$$-B_{\theta n}^a + B_{\theta n}^b = \mu_0 M_{\theta n} \tag{2.56}$$

$$-B_{\theta n}^c + B_{\theta n}^d = -\mu_0 M_{\theta n} \tag{2.57}$$

The vector potential is continuous. (2.35) is rewritten as

$$\begin{bmatrix} 1 & -1 & 0 & 0 & 0 & 0 & 0 & 0 \\ 0 & 0 & 1 & -1 & 0 & 0 & 0 & 0 \\ \frac{n}{R_o} & 0 & 0 & 0 & -1 & 0 & 0 & 0 \\ 0 & -F_{n1} & -G_{n1} & 0 & 0 & 1 & 0 & 0 \\ 0 & -G_{n2} & -F_{n2} & 0 & 0 & 0 & 1 & 0 \\ 0 & 0 & 0 & \frac{n}{R_i} & 0 & 0 & 0 & 1 \\ 0 & 0 & 0 & 0 & -1 & 1 & 0 & 0 \\ 0 & 0 & 0 & 0 & 0 & 0 & -1 & 1 \end{bmatrix} \begin{bmatrix} A_{zn}^a \\ A_{zn}^b \\ A_{zn}^c \\ A_{zn}^d \\ B_{\theta n}^a \\ B_{\theta n}^b \\ B_{\theta n}^c \\ B_{\theta n}^d \end{bmatrix} = \begin{bmatrix} 0 \\ 0 \\ 0 \\ T_{n1}\mu_0(M_{rn} + nM_{\theta n}) \\ T_{n2}\mu_0(M_{rn} + nM_{\theta n}) \\ 0 \\ M_{\theta n} \\ -M_{\theta n} \end{bmatrix} \mu_0 \tag{2.58}$$

where

$$F_{n1} = \frac{n(R_i^{2n} + R_o^{2n})}{R_o(R_i^{2n} - R_o^{2n})} \tag{2.59}$$

$$F_{n2} = \frac{n(R_i^{2n} + R_o^{2n})}{R_i(R_o^{2n} - R_i^{2n})} \tag{2.60}$$

$$G_{n1} = \frac{2nR_i^n R_o^n}{R_o(R_o^{2n} - R_o^{2n})} \tag{2.61}$$

$$G_{n2} = \frac{2nR_o^n R_i^n}{R_i(R_i^{2n} - R_o^{2n})} \tag{2.62}$$

$$T_{n1} = -\frac{1}{n^2 - 1} + \frac{n(R_o^{2n} + R_i^{2n} - 2R_o^{n-1}R_i^{n+1})}{(n^2 - 1)(R_o^{2n} - R_i^{2n})} \tag{2.63}$$

$$T_{n2} = -\frac{1}{n^2 - 1} + \frac{n(R_o^{2n} + R_i^{2n} - 2R_i^{n-1}R_o^{n+1})}{(n^2 - 1)(R_o^{2n} - R_i^{2n})} \tag{2.64}$$

$M_n = M_{rn} + nM_{\theta n}$. When $M_{rn} = M_{\theta n}$, the cylinder generates a strong internal field and the solution to (2.58) is

$$\begin{bmatrix} A_{zn}^a \\ A_{zn}^b \\ A_{zn}^c \\ A_{zn}^d \\ B_{\theta n}^a \\ B_{\theta n}^b \\ B_{\theta n}^c \\ B_{\theta n}^d \end{bmatrix} = \begin{bmatrix} 0 \\ 0 \\ -\dfrac{\mu_0 M_{\theta n}(R_o R_i^n - R_o^n R_i)}{R_o^n(n-1)} \\ -\dfrac{\mu_0 M_{\theta n}(R_o R_i^n - R_o^n R_i)}{R_o^n(n-1)} \\ 0 \\ \mu_0 M_{\theta n} \\ -\dfrac{n\mu_0 M_{\theta n}(R_i R_o^n - R_i^n R_o)}{R_o^n R_i(n-1)} \\ \dfrac{n\mu_0 M_{\theta n}(R_o R_i^n - R_o^n R_i)}{R_o^n R_i(n-1)} \end{bmatrix} \tag{2.65}$$

When $M_{r_n} = -M_{\theta_n}$, the cylinder generates a strong external field and the solution of (2.58) is

$$\begin{bmatrix} A_{zn}^a \\ A_{zn}^b \\ A_{zn}^c \\ A_{zn}^d \\ B_{\theta n}^a \\ B_{\theta n}^b \\ B_{\theta n}^c \\ B_{\theta n}^d \end{bmatrix} = \begin{bmatrix} -\dfrac{\mu_0 M_{\theta n}(R_o^{n+1} - R_i^{n+1})}{R_o^n(n+1)} \\ -\dfrac{\mu_0 M_{\theta n}(R_o^{n+1} - R_i^{n+1})}{R_o^n(n+1)} \\ 0 \\ 0 \\ -\dfrac{n\mu_0 M_{\theta n}(R_o^{n+1} - R_i^{n+1})}{R_o^{n+1}(n+1)} \\ \dfrac{n\mu_0 M_{\theta n}(R_o^{n+1} - R_i^{n+1})}{R_o^{n+1}(n+1)} \\ \mu_0 M_{\theta n} \\ 0 \end{bmatrix} \tag{2.66}$$

At an arbitrary position (r_0, θ_0), where $0 < r_0 < R_i$ and $0 \le \theta_0 \le 2\pi$, applying the homogeneous transfer relations in (2.53) with $\alpha = R_i$ and $\beta = r_0$.

$$\begin{bmatrix} B_{\theta n}^d \\ B_{\theta n}^{r_0} \end{bmatrix} = \begin{bmatrix} \dfrac{n(R_i^{2n}+r_0^{2n})}{R_i(r_0^{2n}-R_i^{2n})} & \dfrac{2nR_i^n r_0^n}{R_i(R_i^{2n}-r_0^{2n})} \\ \dfrac{2nr_0^n R_i^n}{r_0(r_0^{2n}-R_i^{2n})} & \dfrac{n(R_i^{2n}+r_0^{2n})}{r_0(R_i^{2n}-r_0^{2n})} \end{bmatrix} \begin{bmatrix} A_{zn}^d \\ A_{zn}^{r_0} \end{bmatrix} \tag{2.67}$$

From (2.55) and (2.67), we conclude

$$B_{\theta n}^{r_0} = -\left(\frac{r_0}{R_i}\right)^{n-1} B_{\theta n}^d \tag{2.68}$$

27

The system is focusing on the internal field, so apply (2.67) and (2.68) to (2.65). The solutions for the internal magnetic flux density and the magnetic vector potential are

$$B_{\theta n}^{r_0} = \left(\frac{r_0}{R_i}\right)^{n-1} \cdot \frac{n\mu_0 M_{\theta n}(R_o R_i^n - R_o^n R_i)}{R_o^n R_i(n-1)} \tag{2.69}$$

$$A_{zn}^{r_0} = -\frac{r_0^n}{R_i^{n-1}} \cdot \frac{\mu_0 M_{\theta n}(R_o R_i^n - R_o^n R_i)}{R_o^n R_i(n-1)} \tag{2.70}$$

$$\boldsymbol{B} = \nabla \times \boldsymbol{A} = \frac{1}{r} \begin{vmatrix} \boldsymbol{i}_r & r\boldsymbol{i}_\theta & \boldsymbol{i}_z \\ \frac{\partial}{\partial r} & \frac{\partial}{\partial \theta} & 0 \\ 0 & 0 & A_{zn}\sin(n\theta) \end{vmatrix} = \frac{n}{r} A_{zn}\cos(n\theta)\,\boldsymbol{i}_r - \frac{\partial A_{zn}}{\partial r}\sin(n\theta)\,\boldsymbol{i}_\theta \tag{2.71}$$

Taking the same partial differential as in (2.71), which is similar to (2.49).

$$B_{rn}^{r_0} = \frac{n}{r_0} A_{zn}^{r_0} = -\left(\frac{r_0}{R_i}\right)^{n-1} \cdot \frac{n\mu_0 M_{\theta n}(R_o R_i^n - R_o^n R_i)}{R_o^n R_i(n-1)} \tag{2.72}$$

Because $\boldsymbol{B}_n = B_{rn}\cos(n\theta)\boldsymbol{i}_r + B_{\theta n}\sin(n\theta)\boldsymbol{i}_\theta$, the magnetic flux density at an arbitrary position (r_0, θ_0) inside the cylinder is

$$\boldsymbol{B}_n^{r_0} = \left(\frac{r_0}{R_i}\right)^{n-1} \cdot \frac{n\mu_0 M_{\theta n}(R_o^n R_i - R_o R_i^n)}{R_o^n R_i(n-1)}[\cos(n\theta_0)\boldsymbol{i}_r - \sin(n\theta_0)\boldsymbol{i}_\theta] \tag{2.73}$$

For an ideal Halbach cylinder with internal field, the fundamental field solution for a 2-pole mode is given in (2.49), and the solution for the nth harmonics for a $2n$-pole mode is given above in (2.73).

2.2. Magnetic Field Analysis of HABTPM

In pracice, the Halbach cylinder is realized by segmented magnets. Zhu *et al*. indicated that the higher the number of segments is, the better the field distribution is [11]. Based on the discussion in the next chapter, the proposed design is a 2-pole, 10-segment Halbach cylinder as shown in Figure 2.3. Because the permeabilities of the 3D-printed

28

ABS material and the NdFeB magnets are very close to that of the free space, we can

assume μ_0 everywhere. The outer and inner radii are $R_o = 38.175$ mm and $R_i = 31.825$

mm. The average angular width of each magnet is $\Delta = 0.2$ rad, so the average angular

width of the gap between the magnet pieces is $g = \frac{\pi}{10} - \Delta = 0.114$ rad.
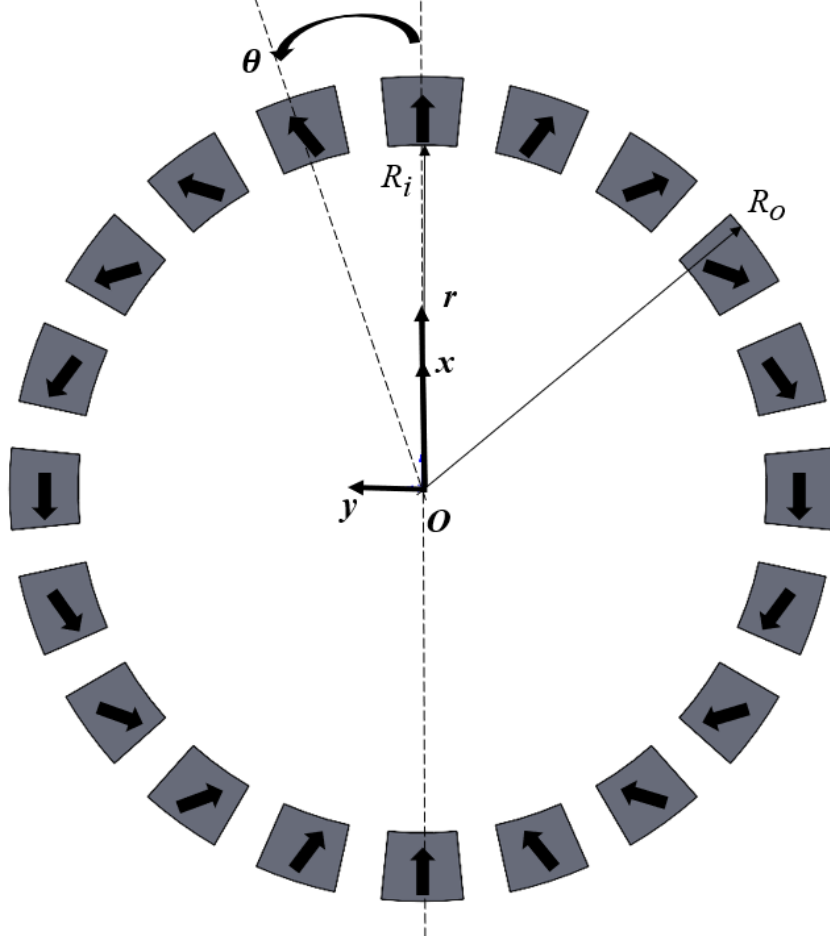

Figure 2.3 Design of a 2-pole, 10-segment Halbach cylinder.

The Fourier series of the magnetization density $\boldsymbol{M}$ is to be found, so we can apply

the result in Section 2.1.3. The nth Fourier harmonics of the r- and θ-components of $\boldsymbol{M}$ in

(2.11) can be calculated as

$$M_{rn} = \frac{1}{\pi} \int_{-\pi}^{\pi} M_r(\theta) \cos(n\theta) \, d\theta \tag{2.74}$$

$$M_{\theta n} = \frac{1}{\pi} \int_{-\pi}^{\pi} M_\theta(\theta) \sin(n\theta) \, d\theta \tag{2.75}$$

Each magnet has the remanence of $\mu_0 M_0$. The distributions of $\boldsymbol{M}$ are shown in Figure 2.4 with the gap of 0 magnetization. With MATLAB, the Fourier coefficients are calculated in Figure 2.5.

As discussed previously, the strong internal magnetic field is generated when M_{rn} has the same value as $M_{\theta n}$. According to Figure 2.5, when $n = 20 \cdot m + 1$, where m is a non-negative integer, the values of M_{rn} and $M_{\theta n}$ are non-zero and the sign of them are the same. When $m > 3$, the magnitude is extremely small compared to the 1st, 21st, and 41st, so they are neglected.

From Figure 2.5, $M_{r1} = 0.6356 M_0$, $M_{r21} = 0.2616 M_0$, and $M_{r41} = -0.12706 M_0$. with the NdFeB PM with $B_{rem} = 1.4$ T, $M_0 = \frac{B_{rem}}{\mu_0} = 1.114 \times 10^6$ A/m. With given data, (2.49) and (2.73) become

$$\boldsymbol{B}_1^{r_0} = 161.89 \text{ mT} \cdot [\cos(\theta_0)\boldsymbol{i}_r - \sin(\theta_0)\boldsymbol{i}_\theta] \tag{2.76}$$

$$\boldsymbol{B}_{21}^{r_0} = 374.44 \text{ mT} \cdot \left(\frac{r_0}{31.825\text{mm}}\right)^{20} [\cos(21\theta_0)\boldsymbol{i}_r - \sin(21\theta_0)\boldsymbol{i}_\theta] \tag{2.77}$$

$$\boldsymbol{B}_{41}^{r_0} = 182.21 \text{ mT} \cdot \left(\frac{r_0}{31.825\text{mm}}\right)^{40} [\cos(41\theta_0)\boldsymbol{i}_r - \sin(41\theta_0)\boldsymbol{i}_\theta] \tag{2.78}$$

Because the armatures are placed in the area of $r < 14.5$ mm, $\boldsymbol{B}_{21}^{r_0}$ and $\boldsymbol{B}_{41}^{r_0}$, which are 5.56×10^{-8} T and 4.02×10^{-15} T at $r = 14.5$ mm, are insignificant in the area according to (2.77) and (2.78). The $\boldsymbol{B}_1^{r_0}$ is dominant, so the magnetic flux density in $r < 14.5$ mm can be considered uniform at 161.89 mT in the $\boldsymbol{i}_x$ direction.
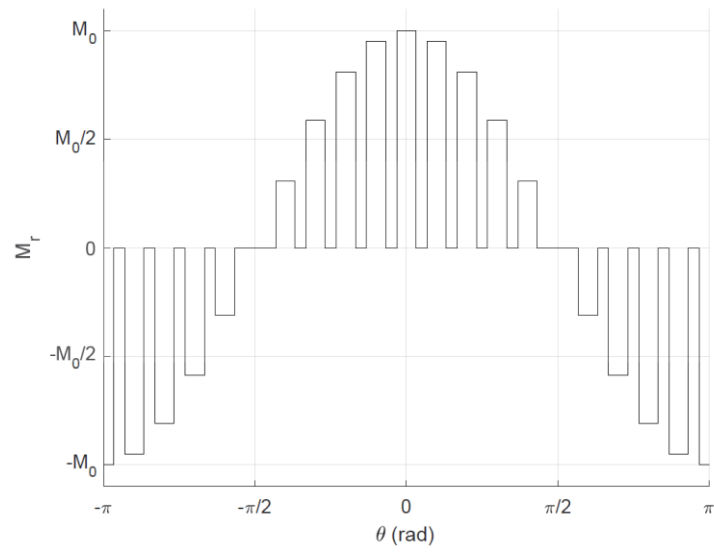
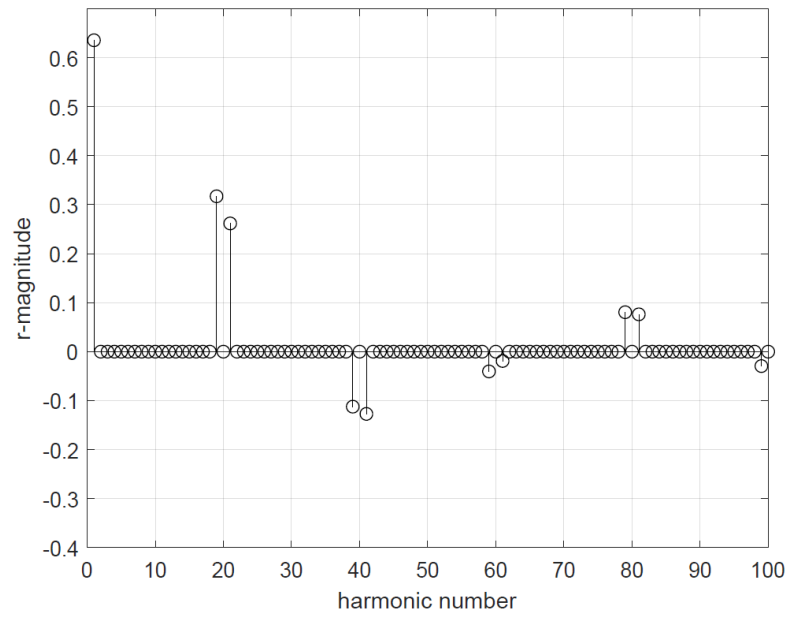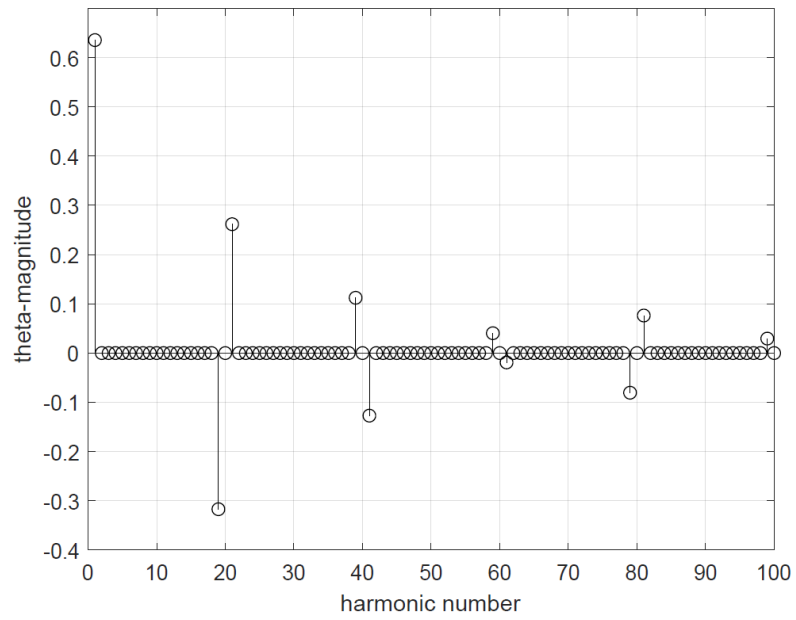**(a)**
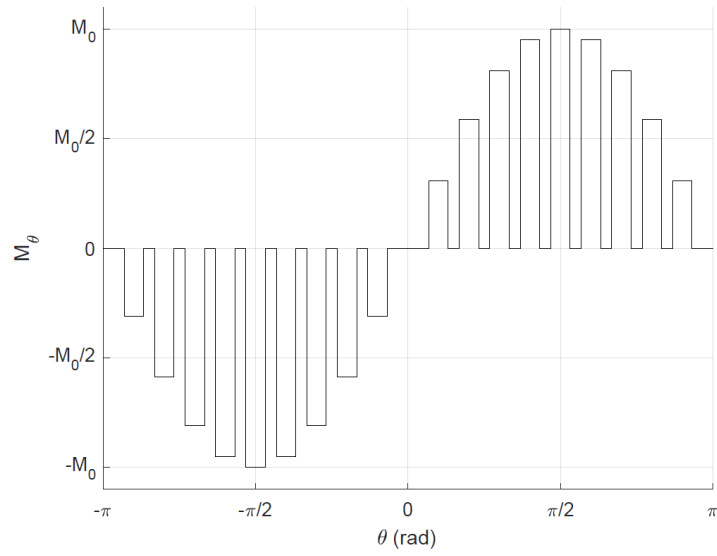
(b)

Figure 2.4 The distributions of the (a) *r* and (b) *θ*-components of *M* with respect to *θ*.

31

(a)

(b)

Figure 2.5 Fourier coefficient of the (a) *r* and (b) *θ*- components of *M*.

2.3. Magnetic Field Simulation of HABTPM

Figure 2.6 (a) shows one of the magnet pieces that would occupy the cylindrical Halbach magnet array. However producing the magnets with these circular curvatures would be costly, and magnetizing them in an oblique angle is very challenging. In a practical design, they are replaced with the magnets with a square cross-section with the magnetization vector pointing face to face as shown in Figure 2.6 (b). An FEA was conducted to verify with the theoretical development presented in the previous section and ensure the error is acceptable. The simulation software is Finite Element Method Magnetics (FEMM), which is a free software package [18]. The FEA result is shown in Figure 2.7.
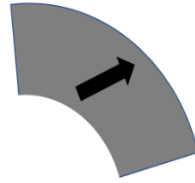
(a)
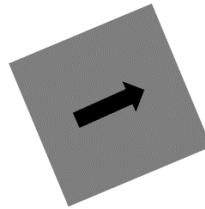
(b)
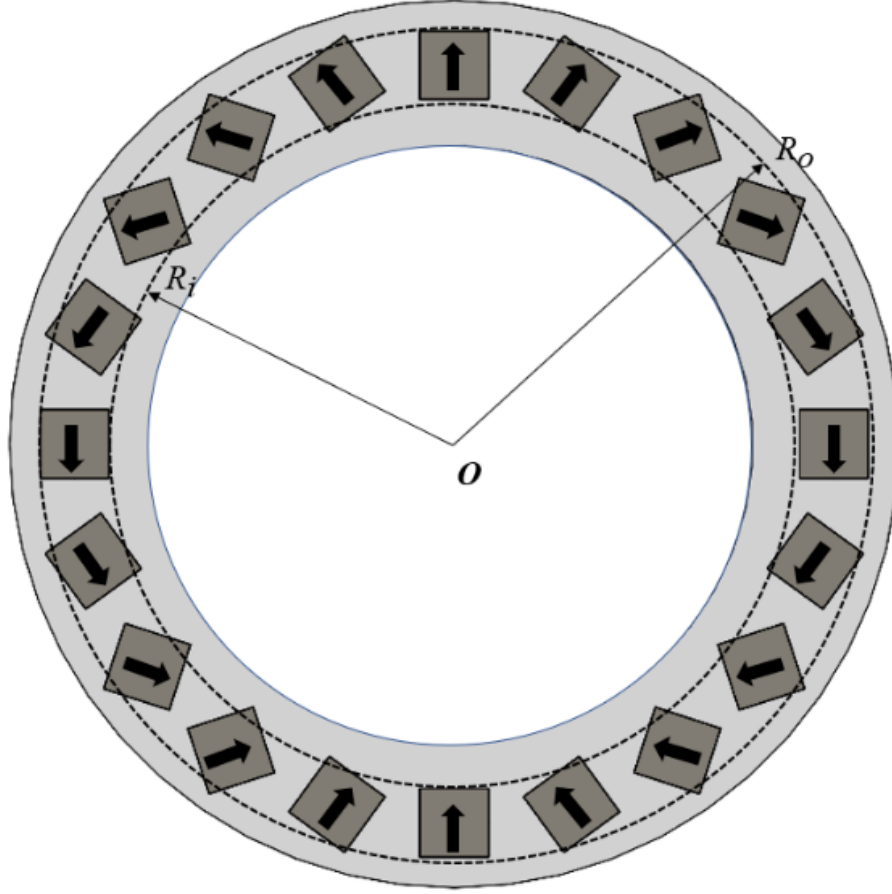
(c)

Figure 2.6 (a) An ideal magnets in a Halbach cylinder, (b) replacement of the magnet with a square cross-section, and (c) actual placement in the HABTPM.

The magnitude of the magnetic flux density inside the Halbach cylinder of $r < 13$ mm is 157 mT, which is very close to the theoretical result of 162 mT, and has the x-component only. Hence, the motor torque $\boldsymbol{\tau} = \int_V \boldsymbol{r} \times (\boldsymbol{J} \times \boldsymbol{B})\, dV$, where $\boldsymbol{J}$ is the current density of the stator current occupying the volume V that can be easily calculated.

Figure 2.7 A magnetic flux density and flux line result by FEM.
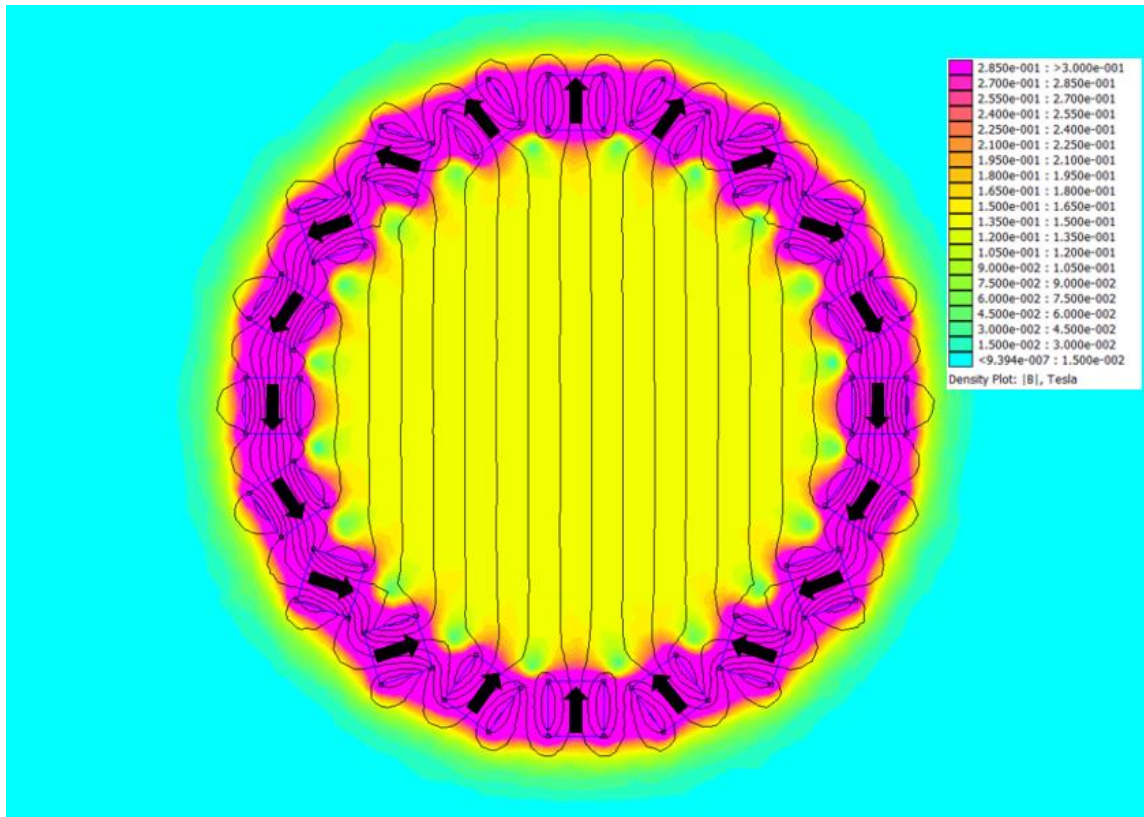
3. MECHANICAL DESIGN AND ELECTRONIC CIRCUIT DESIGN

This chapter begins with the conceptual design of the HABTPM. In the first section, the evolution of the conceptual design is explained in detail. The design is based on 3D-printed ABS plastic material. The limitation of this material and the detail design of the motor is illustrated in Section 3.2. The sensors for the system and the circuit design for Arduino microcontroller is processed in Section 3.3.

3.1. Conceptual Design

The conceptual design starts with the magnet placement in Figure 1.2. The original design has a 30° rotation of a 2-pole Halbach cylinder, but inner space was too narrow to place Hall-effect and temperature sensors together. The Hall-effect sensors are utilized to detect the magnetic flux density while the temperature sensors are used to sense winding temperature. The temperature detection is essential because the 3D-printed material has the difficulty to maintain rigidity beyond 100°C due to the heat generated by the current carrying coils on the stator. The diameter of the external Halbach cylinder must be enlarged from $d = 72$ mm to $d = 82$ mm. Figure 3.1 shows the development of the prototyping ideas. The magnets have dimension of 6.35×6.35×38.1 mm, so a 30° rotation with 12 magnets has significant gaps between each magnet. In this case, the average gap between each magnet is very large compare to the average width of the magnets, so extra magnets are added to the cylinder. The maximum number of magnets placed in this cylinder is 20, so the final design becomes an 18° rotation with 20 magnets 2-pole Halbach

cylinder as shown in Figure 3.1(c). In the next section, the design this prototype as the final design is illustrated in detail.
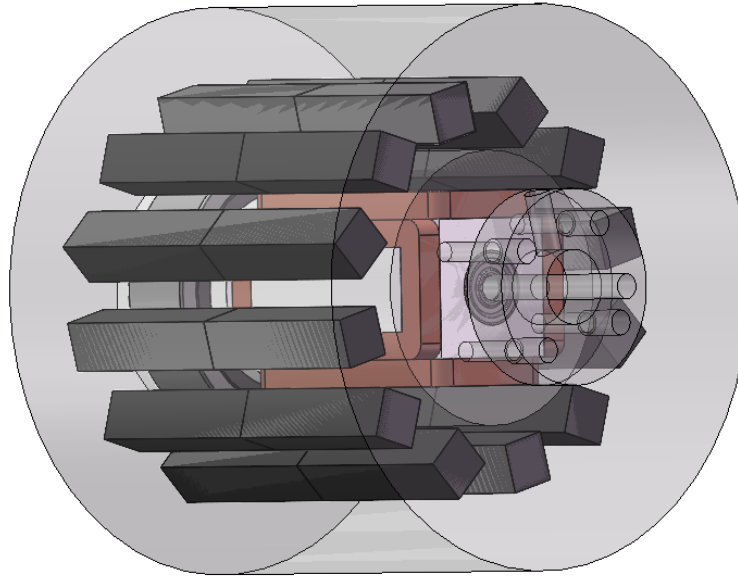
(a)
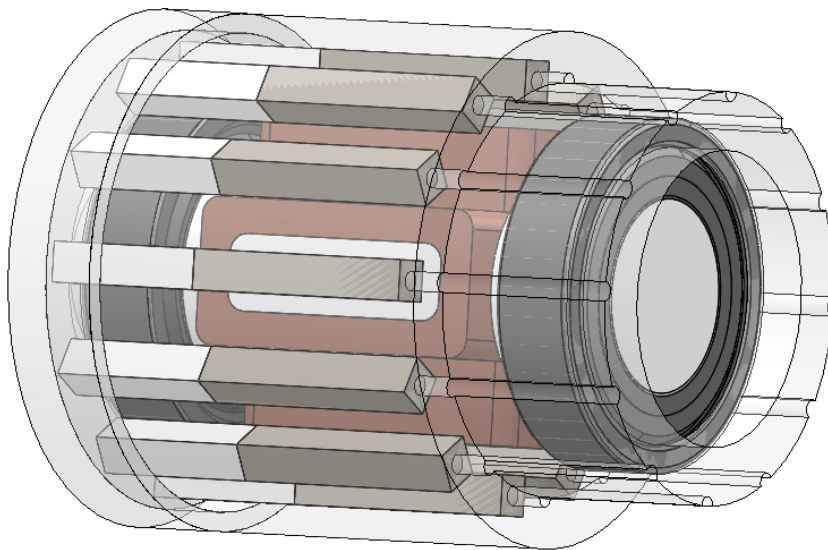
(b)
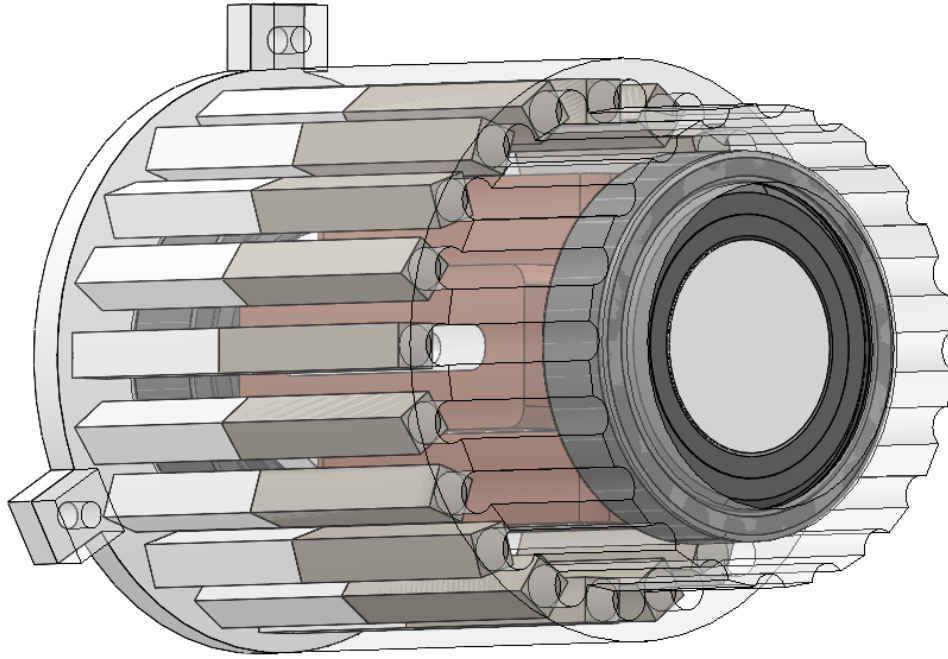
(c)

Figure 3.1 The improvement of the 2-pole segment prototype Halbach cylinder design. (a) The prototype with 30° rotation 2-pole segment Halbach cylinder, (b) The enlarged prototype with 30° rotation 2-pole segment Halbach cylinder, (c) The enlarged prototype with 18° rotation 2-pole segment Halbach cylinder.

3.2. Mechanical Design

The final design is a 2-pole, 10-segment Halbach cylinder. The magnetic flux density of this structure is calculated in Chapter 2. Figure 3.2 shows the section view of the HABTPM. There are 20 magnets placed in the outside cylinder. Temperature sensors and Hall-effect sensors are placed at the side and the top of the coils in both phases. The ball bearings are 30-mm-bore-diameter, 55-mm-outside-diameter, and 13-mm-width steel

38

ball bearings. The cap on the left in Figure is to hold the magnets and the stator inside the

motor.
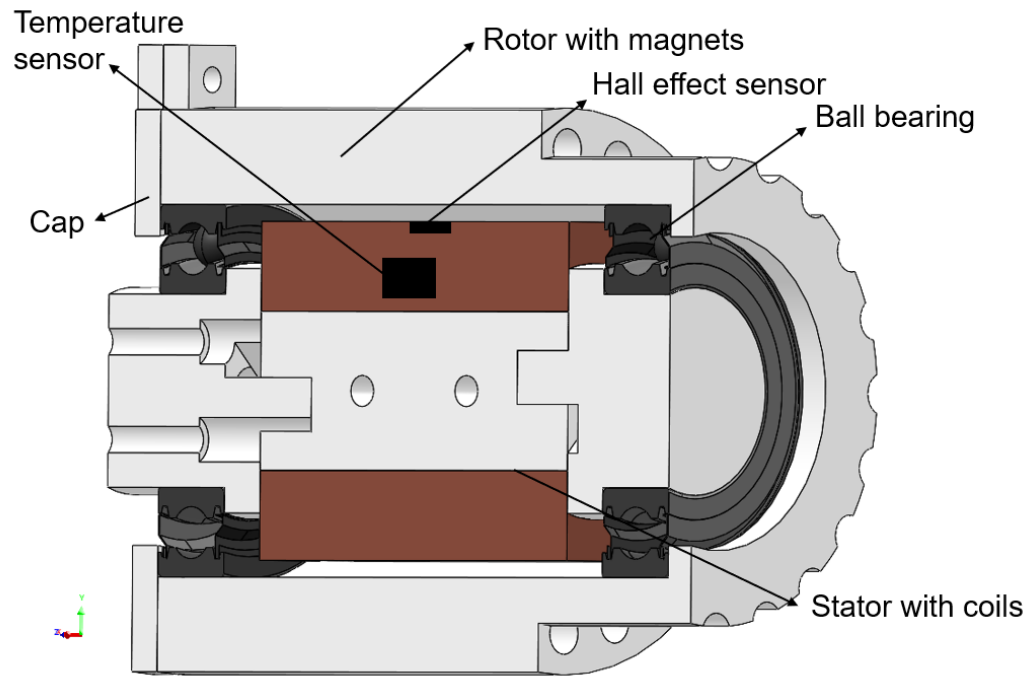
Figure 3.2 Section view of the motor.

The engineering drawing of the bearing is in Figure 3.3. All units are in mm. The

technical detail of the ball bearing is given in Table 3.1. The bearings are utilized to hold

the stator inside and let the outer cylinder with magnets rotate smoothly.

Table 3.1 Technical details of the ball bearings [12].

Item	Radial Ball Bearing	Temperature range	−28.89°C to 121.11°C
Bore Dia.	30 mm	Cage Material	Pressed Steel
Outside Dia.	55 mm	Shield Material	Rust-Resistant Metal
Width	13 mm	Load Capacity	13,216 N
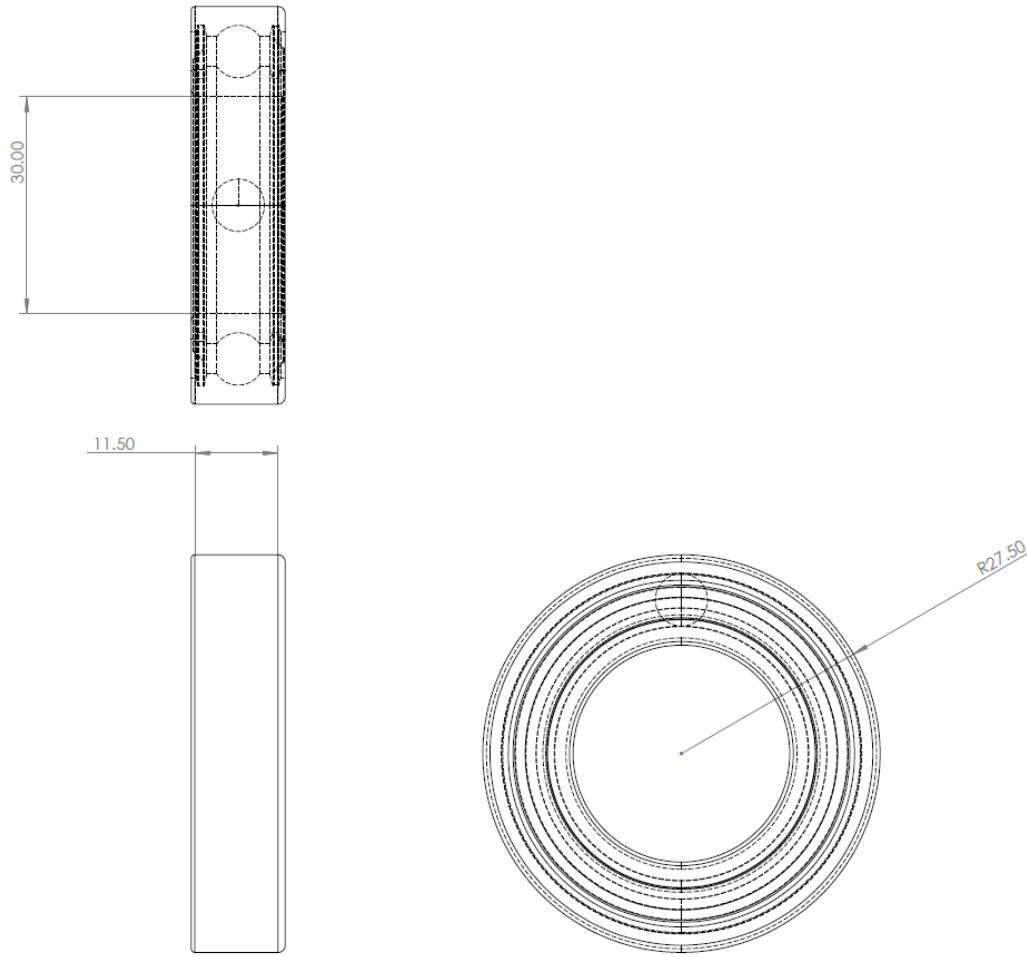
Figure 3.3 Engineering drawings of the ball bearing [12].

In Chapter 2, the inner and outer radii of the magnets array were given. In the rotor design, the inner and outer diameters are slightly larger than the one of the magnets array. The design parameters are shown in the engineering drawing in Figure 3.4. All units are in mm. Due to strong force between each magnets, the outer diameter of the cylinder is 82 mm, which is greater than $D_0 = 2R_0 = 76.35$ mm, while the inner diameter of the cylinder is 55 mm, which is less than $D_i = 2R_i = 63.65$ mm in Section 2.2. The diameter of the part that holds the bearing without magnets is reduced to 67.77 mm.

Figure 3.4 Engineering drawings of the rotor that contains the Halbach magnet cylinder.

The magnet cylinder on the rotor is aligned with the center of the coil, so, in torque calculation, the effective length is equal to the magnet length. Figure 3.5 shows that the coils are aligned with the magnets. The length of the magnets L_0 is 38.1 mm. The ball

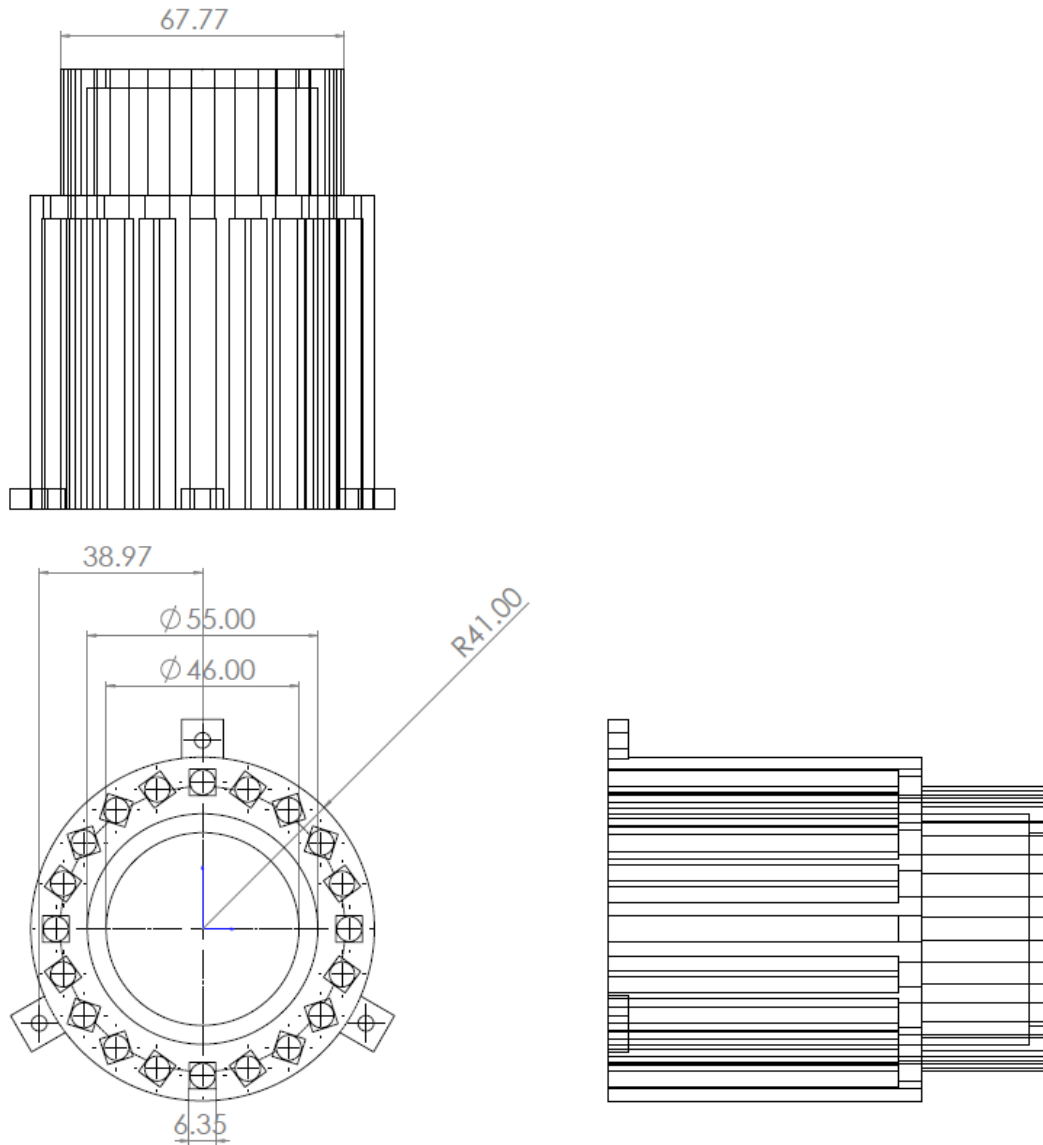bearings are made of steel, so they must be placed away from the magnets shown in Figure 3.5.
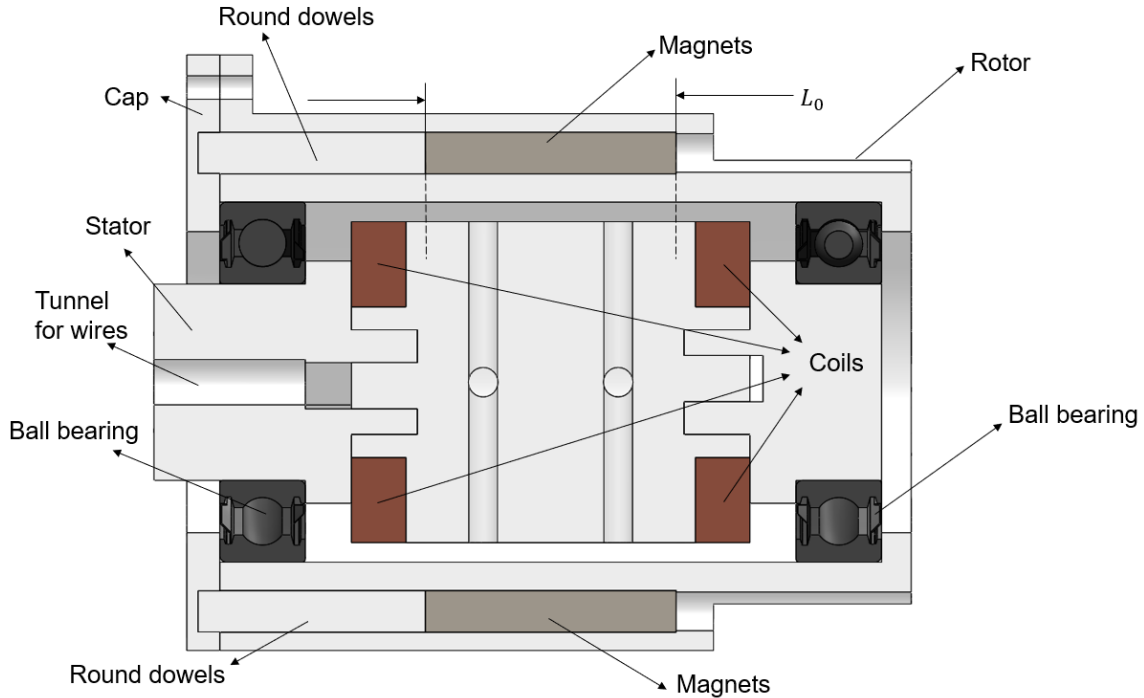
Figure 3.5 Section view of the motor in the *y-z* plane.

The first step to assemble the motor is inserting all the magnets into the designated position discussed in Section 2.3. Then insert round dowels to fix them at the center. After four coils were fixed on the stator, the bearings were placed on the two sides of the stator and then all interior parts were inserted into the hollow of the rotor. The last step is fixing cap with screws. Because the material of rotor and stator are 3D-printed ABS material with the resolution of 0.1 mm, the gap between the rotor and the ball bearings that causes alignment issues was inevitable. This might cause relatively large friction.

Figure 3.6 (a) shows the appearance of the armature/stator with coils. Each phase consists of two internally connected coils. Figure 3.6 (b) shows the dimension of the coil.

The coil is made of American wire gauge (AWG) #22 wires, which can carry 7 A current at 75°C [19], with 7 layers. Each layer has 15 turns. The average distance between each layer is around 0.7 mm which is larger than the diameter of the wires because there are some glues and tapes to fix each layer. In this case, the coils only have a fill factor of 52.66%.

(a)

(b)

7 layers

$w = 5$ mm

15 turns

$h = 13$ mm

$d_c = 6.45mm$
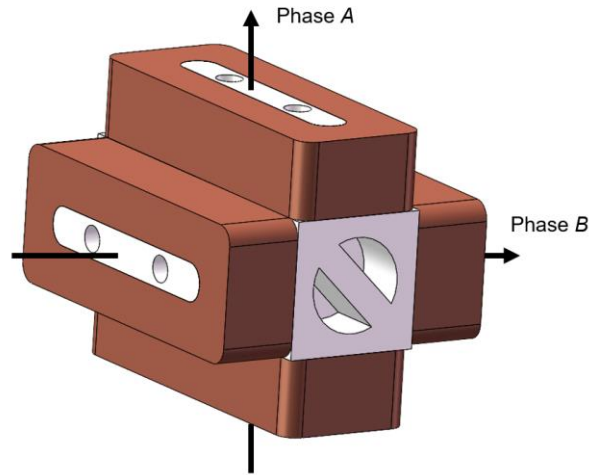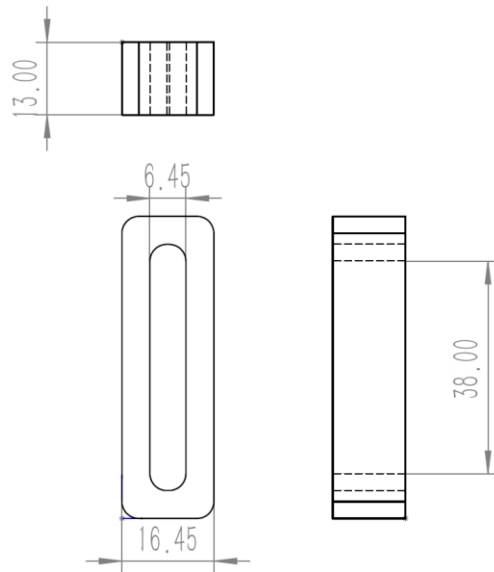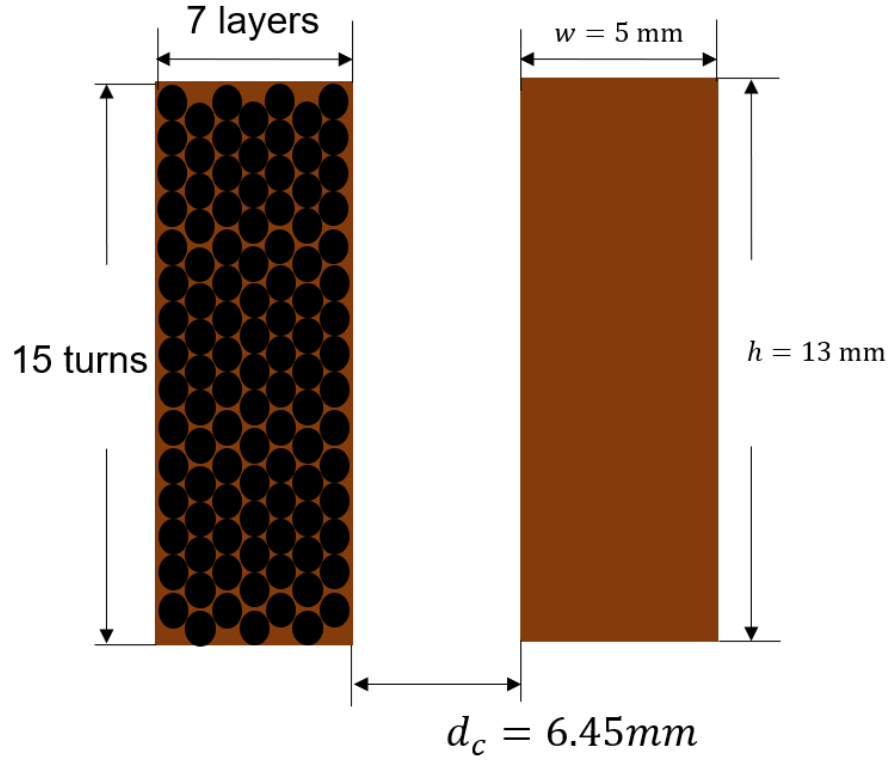
(c)

Figure 3.6 (a) The design of the armature, (b) the engineering drawing of the coil, and (c) section view of the coil.

As shown in the Figure 3.7, the Hall-effect sensors are place at the center of the coil in each phase. The temperature sensors are placed directly on the surface of the coils. The distance between the top and the bottom surfaces is 29 mm. In Section 2.2, we have already discussed that the magnetic flux density inside the Halbach cylinder of $r < 14.5$ mm is uniform, so the Hall-effect sensors placed on the face of the coils should detect a sinusoidal magnetic flux density with a period of 2π with respect to angle as the rotor, a Halbach cylinder, rotates.

Figure 3.7 The coils on the armature and the placement of the sensors.

3.3. Electronic Circuit Design and Hardware Implementation

3.3.1. Sensors

The magnitude of the magnetic flux density in the coils are uniform at 157 mT according to the result in Section 2.3, so the Hall-effect sensor selected for this range is

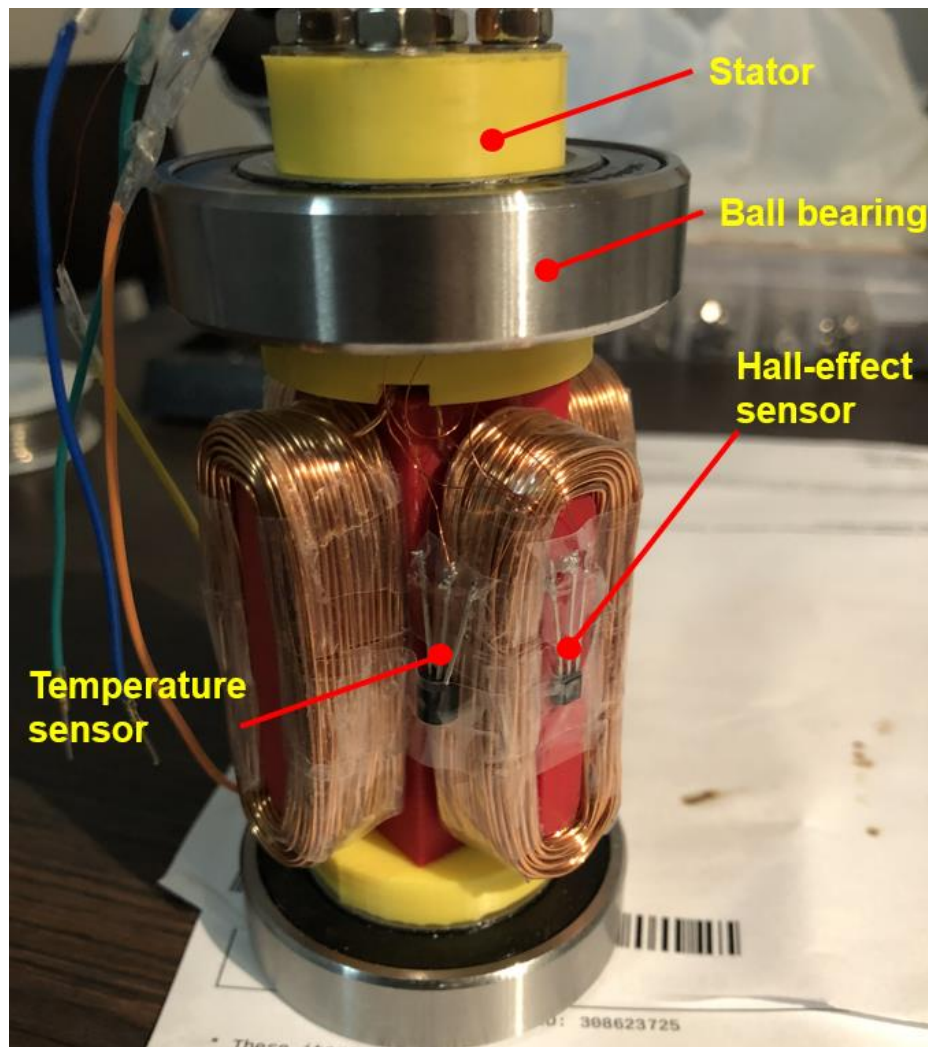DRV5055A4. According to the datasheet of the sensor, it can detect the range of ± 169 mT at a 5-V output voltage with sensing bandwidth of 20 kHz [13]. The power V_{cc} for Arduino Mega 2560 is 5 V, and the analog-to-digital converter (ADC) voltage swing is also 5 V, so the V_{cc} for the sensor is set up as 5 V. The relation between the voltage output V_{OUT} and the magnetic flux density B given by the datasheet is [13].

$$V_{OUT} = V_Q + B \cdot Sensitivity(25°C) \cdot [1 + S_{TC}(T_A - 25°C)] \qquad (3.1)$$

V_Q is half V_{cc}, which is 2.5 V. T_A is the ambient temperature, which is collected by the temperature sensor of each coil phase. According to the data sheet, sensitivity at 25°C is 12.5 mV/mT, and S_{TC} is 0.0012/°C [13]. Solving for B,

$$B = \frac{V_{OUT} - 2.5V}{[1 + 0.0012/°C \cdot (T_A - 25°C)]12.5 mV/mT} \qquad (3.2)$$

The temperature sensor is TMP36, which has sensing range of $-40°C$ to 125°C and provides a 750 mV output at 25°C with the scaling factor of 10mV/°C [14]. Then, the relation between the temperature T and the output voltage V_T is

$$T = V_T \cdot 0.1°C/mV - 50°C \qquad (3.3)$$

The temperature is not only for calculating the magnetic flux density, but also for safety. If the temperature exceeds 100°C due to the heat generated by the current-carrying coils, the structure with 3D-print ABS material and the ball bearing may be damaged. If the temperature reaches 80°C, the system will be shut down to protect the motor.

The 10-bit ADC on Arduino Mega 2560 has a 5-V input voltage swing. The resolution is then 4.89 mV. From (3.2), we have the resolution of 0.39 mT at 25°C and 0.36 mT at 80°C.

3.3.2. Voltage Shifter Circuit and Amplifier Circuit

Arduino is not able to generate analog output by itself, so a digital-to-analog converter (DAC), MCP4725, is introduced to the system. The I²C interface of the device is easy to communicate with the host device, which is Arduino Mega 2560. With 12-bit resolution, it can generate analog voltage between 0 to 5V with the resolution of 1.22 mV [15].
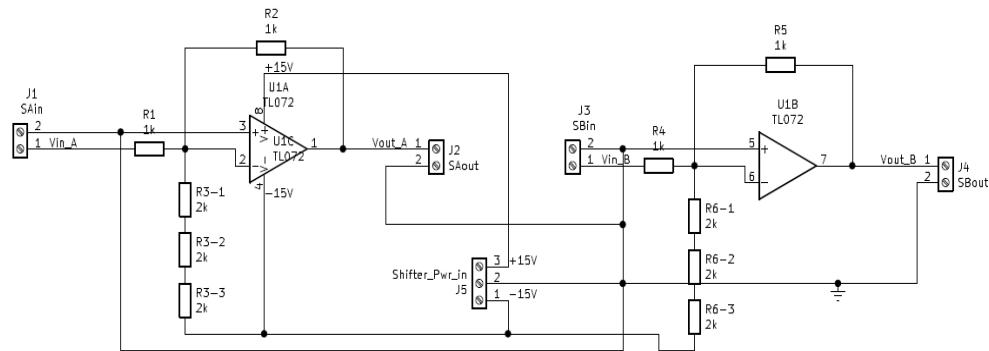
(a)

(b)

Figure 3.8 (a) The diagram of voltage shifter circuit and (b) the hardware of the circuit.

The DAC MCP4725 only generate positive voltage. The motor requires both positive and negative current inputs. A voltage shifter circuit is designed in Figure 3.8. As shown in the figure, $R_1 = R_2 = R_4 = R_5 = 1 \text{ k}\Omega$, $R_3 = R_6 = 6 \text{ k}\Omega$. The circuit has two identical channels for each phase of the motor.

The relation between input the V_{in} and the output V_{out} is then

$$V_{out} = V_{in} - 2.5 \text{ V} \tag{3.4}$$

The input range is 0–5 V from DAC MCP4725, so the output range is –2.5 to 2.5 V. These two voltage shifter channels are connected to power amplifier circuits. For power amplifier circuits, two PA12A power operational amplifier from Apex Microtechnology with the advantage of good power rating and thermal stability are used.

The design of power amplifier circuit is shown in Figure 3.10. The original circuit was designed by Kim and Nguyen [4]. I modify the circuit to fulfill the requirement. Only one channel is shown in figure, and the other channel is a duplication of this one. The inductance of each phase $L_a = 152 \text{ µH}$. The resistance of the coils of each phase $R_a = 1.5 \text{ }\Omega$. All capacitors have the same capacitance of 10 nF. Resistors $R_1 = R_2 = R_3 = R_4 = R_5 = R_6 = R_7 = R_8 = R_9 = 10 \text{ k}\Omega$. There are two parallel resistors $R_{10} = 1 \text{ }\Omega$ with maximum power of 10 W in the part of current output. C_3 and R_6 are set as the function of proportional-integral (PI) controller to eliminate the steady-state error of the current output. The transfer function of the circuit between voltage input $V_{in}(s) = V_2(s) - V_1(s)$ and the current output $I_a(s)$ in the diagram is

$$\frac{I_a(s)}{V_{in}(s)} = \frac{R_3 \cdot R_7 \cdot (R_9 + R_8)(R_6 C_3 s + 1)}{R_1 R_5 [\frac{R_{10}}{2}(R_9 + R_8)(R_6 C_3 s + 1) + R_9 R_7 C_3 (L_a s + R_a + \frac{R_{10}}{2})s](R_3 C_2 s + 1)} \tag{3.5}$$

48
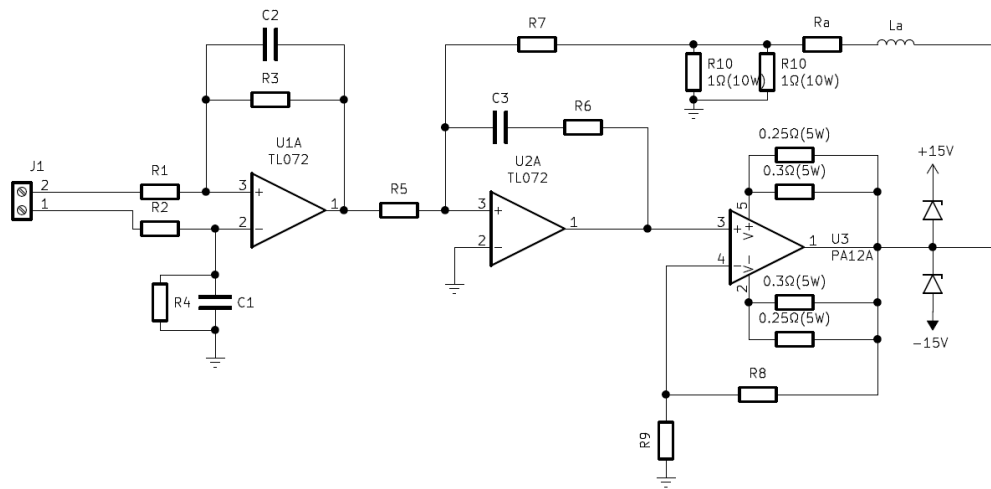
(a)

(b)

Figure 3.9 (a) The diagram of the power-amplifier circuit and (b) the hardware of the circuit with two channel.

49

V_1 is connected to the ground while V_2 is connected to V_{out} in (3.4). The step response and the Bode plot of the amplifier circuit are shown in Figures 3.11 and 3.12.
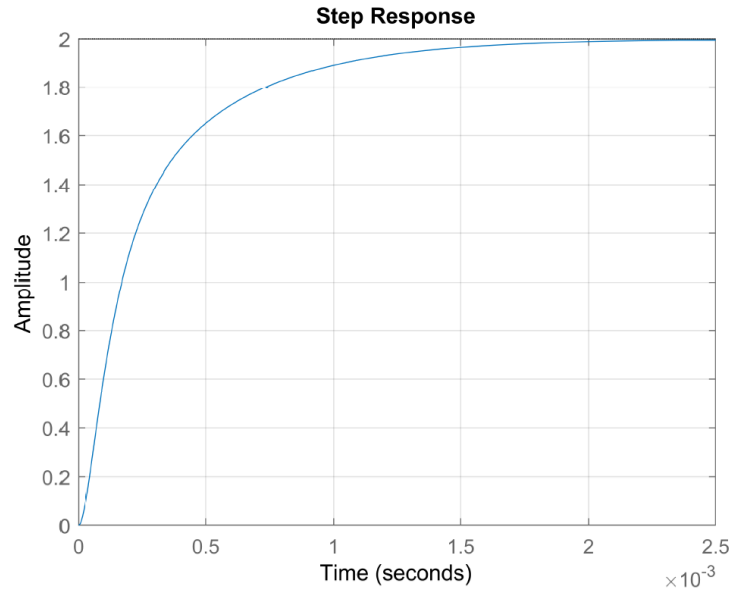
Figure 3.10 Step response of the power amplifier circuit.
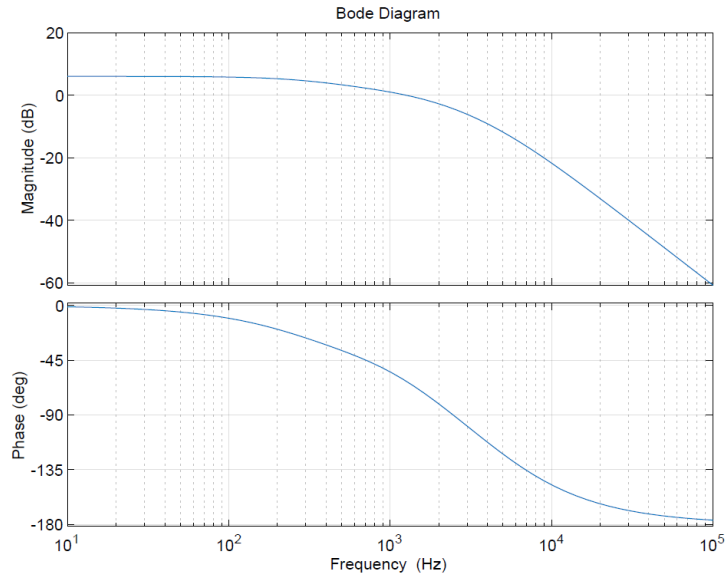
Figure 3.11 Bode plot of the power amplifier circuit.

The settling time is less than 2.5 ms, which means the system has good response. The range of input voltage is –2.5 to 2.5 V with resolution of 1.22 mV. According to Figure 3.11, the range of output current is –5 to 5 A with the resolution of 2.44 mA. Although the amplifier circuit has theoretically maximum output at 5 A, it can never reach it because, according to the datasheet, the current output limit at ±15 V is set as 4.2 A [16]. For safety concern, the current range is set within –4 to 4 A by the program. In conclusion, the system has the ability to generate accurate current within the range of –4 to 4 A with a resolution of 2.44 mA.

The motor is running below 10 Hz. According to the bode plot in Figure 3.12, the phase lag is less than 1.2°, so the delay in the dynamics performance of the power amplifier is negligible. Because the power amplifier circuit generates the current output with a PI controller eliminating the error, the back emf generated by the motor can also be neglected in the torque calculation in the next chapter.

4. DYNAMICS AND CONTROL

4.1. Motor Dynamic Analysis

Figure 4.1 shows the section view in the *x-y* plane of the HABTPM. The inner cylinder has two phases of the armature with four coils. The top and bottom coils are designated as phase *A*. The angle between the magnetic axis of phase *A* and the magnetic axis of the Halbach cylinder is ψ. The left and right coils are designated as phase *B*. The rotor contains twenty permanent magnets in the Halbach cylinder which generates the uniform flux density within the cylinder as shown in Figure 2.7.
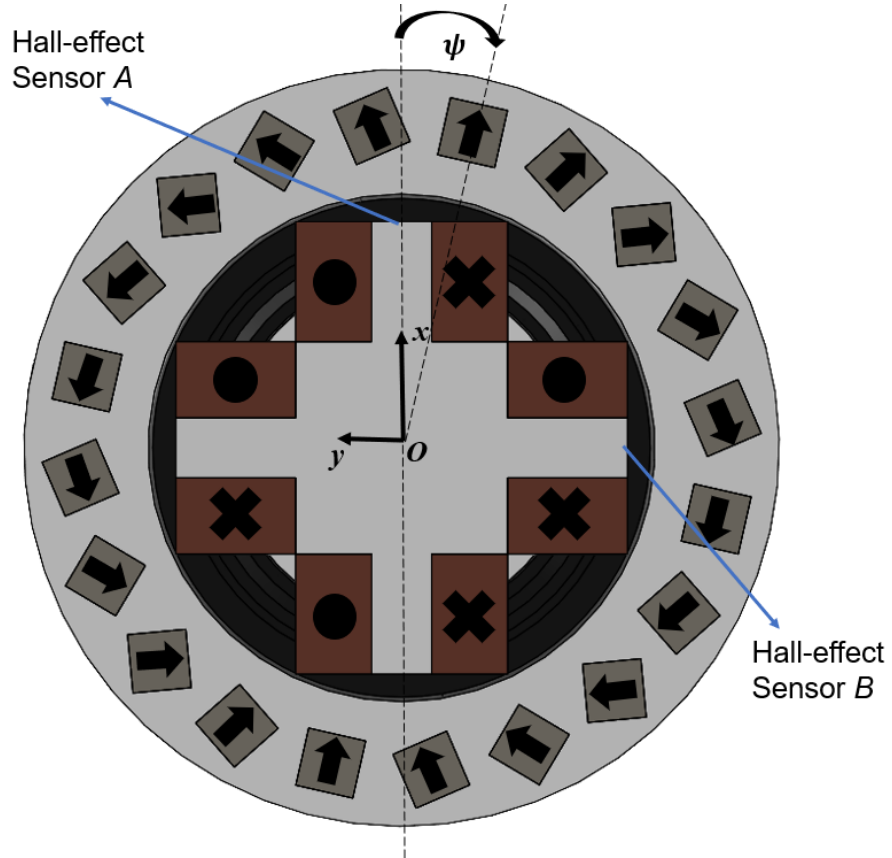

Figure 4.1 Section view in the *x-y* plane of the HABTPM

The positive reference currents carried by the coils are shown in Figure 4.1. The self-inductances of phases A and B are L_0 measured as 152 μH in the HABTPM. Since the two phases are perpendicular, there is zero mutual inductance. In (4.1), ϕ_m is the maximum net magnetic flux penetrating the coil area, n is number of turns, B is uniform magnetic flux density inside the Halbach cylinder, and a_j is the area of the jth turn. The coils in phase B are identical to those in phase A except for a 90° phase difference.

$$\phi_m = B \cdot \Sigma\, a_j \tag{4.1}$$

Then, the electrical terminal relation is derived in

$$\begin{bmatrix} \lambda_A \\ \lambda_B \end{bmatrix} = \begin{bmatrix} L_0 & 0 \\ 0 & L_0 \end{bmatrix} \begin{bmatrix} i_A \\ i_B \end{bmatrix} + \begin{bmatrix} \cos\psi \\ \sin\psi \end{bmatrix} \phi_m \tag{4.2}$$

where i_A and i_B are the phase A and phase B currents. The co-energy W' stored in the HABTPM can be written as equation (4.3). The torque τ_m generated by the motor is derived by (4.4)–(4.5).

$$W' = \frac{1}{2}L_0 i_A^2 + \frac{1}{2}L_0 i_B^2 + \phi_m(i_A\cos\psi + i_B\sin\psi) \tag{4.3}$$

$$\tau_m = \frac{\partial W'}{\partial \psi}\Big|_{i_A,\ i_B} \tag{4.4}$$

$$\tau_m = \phi_m(-i_A\sin\psi + i_B\cos\psi) \tag{4.5}$$

The torque in (4.5) is proportional to the current input $I(t)$ with the following commutation

$$i_A = -I(t)\sin\psi \tag{4.6}$$

$$i_B = I(t)\cos\psi \tag{4.7}$$

53

Assume the system has the damping torque τ_c with the damping coefficient c and the Coulomb friction torque τ_f with the coefficient K_f, then the mechanical equation of motion can be derived as (4.8) and (4.9). J_m is the moment of inertia of the HABTPM's rotor.

$$J_m\ddot{\psi} + \tau_c + \tau_f = \tau_m \tag{4.8}$$

$$J_m\ddot{\psi} + c\dot{\psi} + K_f\text{sgn}(\dot{\psi}) = \phi_m I(t) \tag{4.9}$$

4.2. Parameter Calibration

4.2.1. Parameters for Torque and Friction

When $\psi = 0$, $i_A = 0$ and $i_B = I$, the torque $\boldsymbol{\tau}_m$ on the rotor is opposite to the torque $\boldsymbol{\tau}_s$ on the stator. According to the equation in Section 2.3 and Figure 4.2,

$$\boldsymbol{\tau}_m = -\boldsymbol{\tau}_s = -4 \cdot \int_V x\boldsymbol{i}_x \times (J\boldsymbol{i}_z \times B\boldsymbol{i}_x)\, dV \tag{4.10}$$

where $J = \frac{k \cdot I}{wh}$, where k is the total turns of each coil. There is a factor of 4 because this volume integration is over one half of the effective volume of a coil and there are two coils per phase. Evaluating the integral,

$$\boldsymbol{\tau}_m = 4 \int_{x=d_c/2}^{w+d_c/2} JBl_0 hx\, dx\, (-\boldsymbol{i}_z) = JBl_0 h \left[\left(w + \frac{d_c}{2}\right)^2 - \left(\frac{d_c}{2}\right)^2\right](-\boldsymbol{i}_z) \tag{4.11}$$

where $\boldsymbol{i}_z$ is the opposite direction of the $\boldsymbol{\psi}$.

$$\tau_m = 2kIBl_0(w + d_c) \tag{4.12}$$

So $\phi_m = 2kBl_0(w + d_c)$. The parameter ϕ_m can be found to be 1.43×10^{-2} Wb with $B = 157$ mT, $l_0 = 38$ mm, $w = 5$ mm, $d_c = 6.45$ mm, and $k = 15 \cdot 7 = 105$. The

54

section view of the coil is shown in Figure 4.2. The maximum theoretical pull-out torque that the HABTPM can generate is $\tau = \phi_m I = 0.057$ N·m at the current input of 4 A.

Figure 4.2 Section view in the *x-y* plane of the stator when $\psi = 0$.

With a constant maximum current input, in steady state at a certain speed, (4.9) becomes

$$I = \frac{c}{\phi_m}\dot{\psi} + \frac{K_f}{\phi_m} \tag{4.13}$$

The angular velocity of the motor $\dot{\psi}$ is measured with various coil current to find out damping torque τ_c with damping coefficient c and Coulomb friction torque τ_f with coefficient K_f. The test result is shown in Figure 4.3. From Figure 4.3 and $\phi_m = 1.43 \times 10^{-2}$ Wb , we have $c = 1.23 \times 10^{-3}$ N·m·s, and Coulomb friction torque $K_f =$

2.05×10^{-2} N·m. The R^2 value of this linear fit is 0.9965, which means that the relation is highly linear.
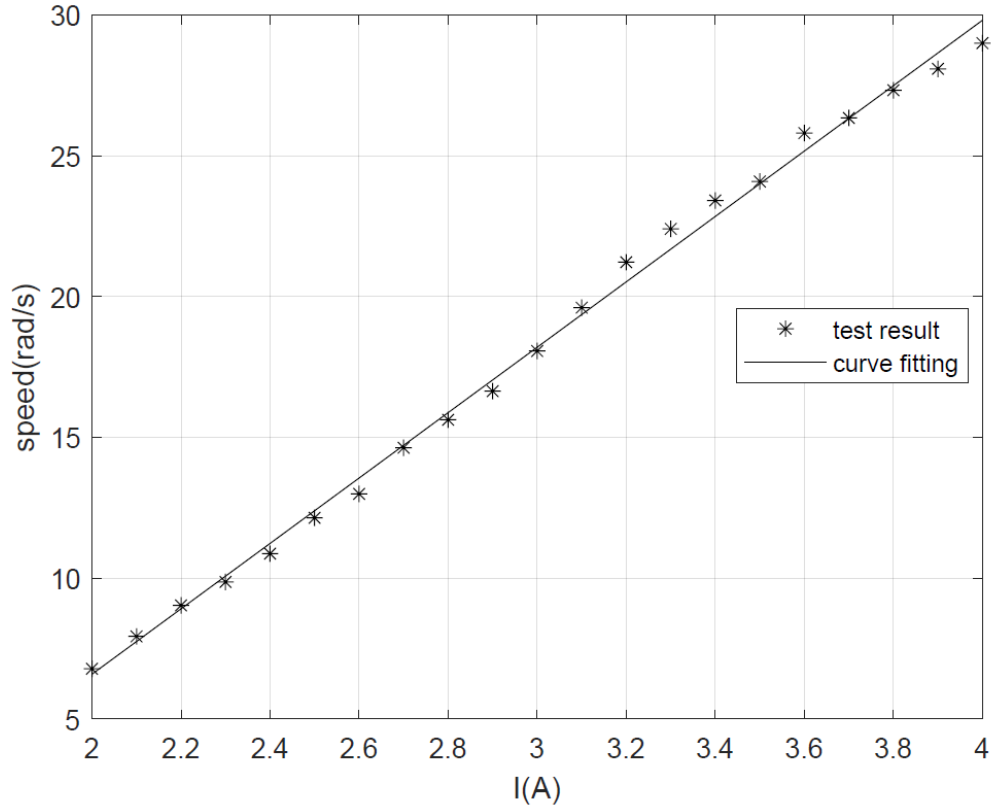
Figure 4.3 Motor speed with different current input.

4.2.2. Position Calibration and Sensing

With the two Hall-effect sensors placed on the faces of the phase *A* and phase *B* coils with a 90° phase difference, the rotor position can be determined. A protractor was installed above the motor as shown in Figure 4.4 to verify the angular position with the reading from the Hall-effect sensor. The Halbach cylinder was rotated with 5° each time manually. The test result of the magnetic flux density of each angular position is shown in

Figure 4.5. The test result shows that the designed Halbach cylinder gives a sinusoidal magnetic flux density with period of 2π and have a maximum magnetic flux density of 162.8 mT, which is consistent with the theoretical result calculated in Section 2.2 and the FEA result in Section 2.3.
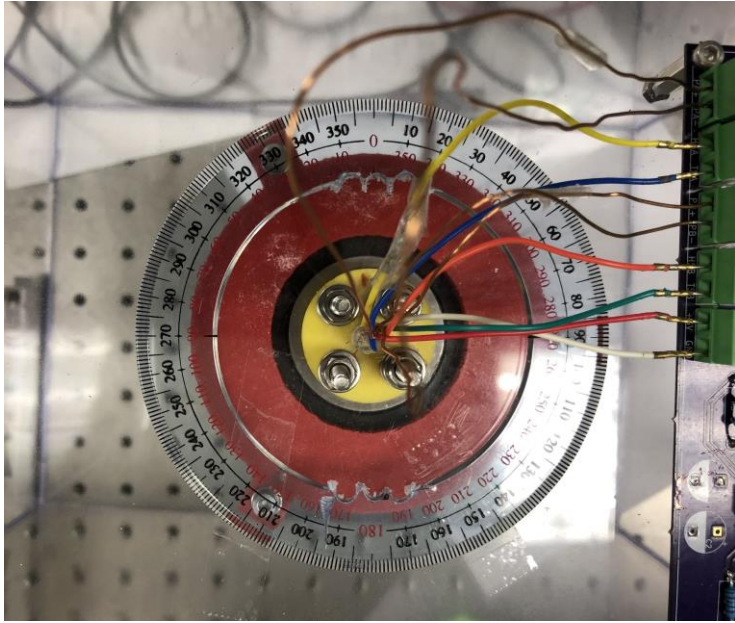
Figure 4.4 The motor with protractor.
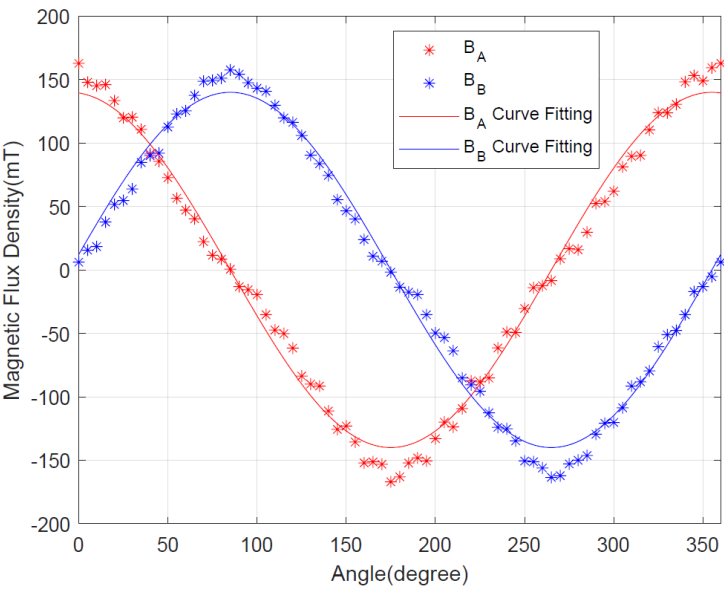
Figure 4.5 Magnetic flux density verification with 5° incremental rotation of the HABTPM.

Although the measurements match well with the sinusoidal function to denote the angular position, they are fitted to four linear functions

$$\psi = a_f B_f + b_f \qquad (4.14)$$

ss shown in Figure 4.6. In (4.4), ψ is the angular position of the motor, B_f is the magnetic flux density chosen from phase A or phase B depending on the values, and a_f and b_f are fitting constants.
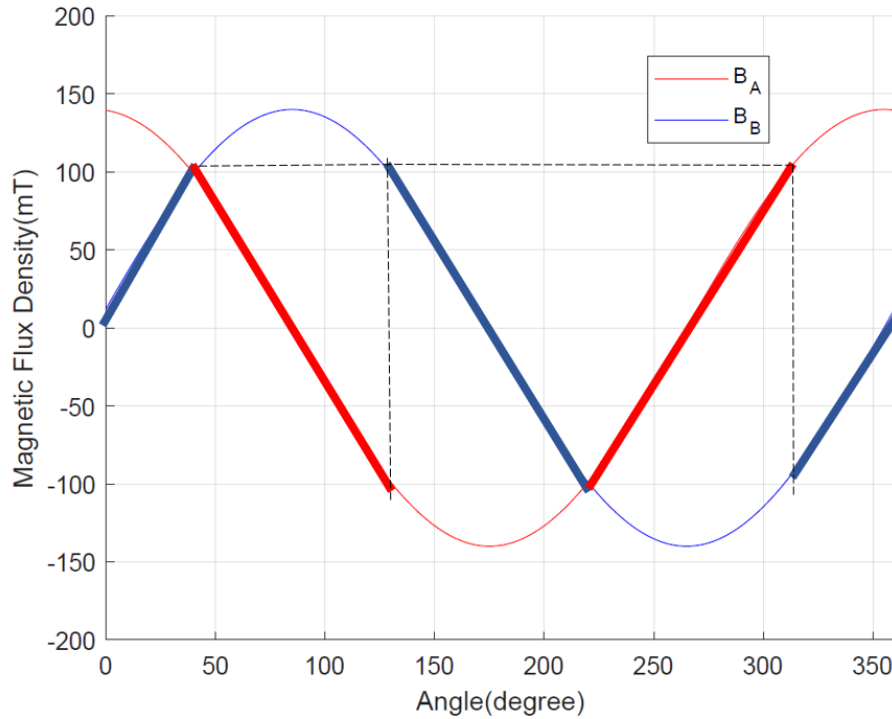
Figure 4.6 The transfer relation between magnetic flux density and the degree

From the calibration, the parameters in (4.14) are given in Table 4.1. Because the rotor and the stator are ABS 3D-printing materials with the resolution of 0.1 mm,

misalignment might occur during fabrication and assembly, the values of a_f and b_f might

be slightly different with the values given in Table 4.1 in real case.

Table 4.1 Parameters of the linear fit in (4.14) under various conditions.

Condition	Parameters
$B_A > 110$ mT, 0 mT $< B_B < 110$ mT	$B_f = B_B$, $a_f = 0.41°/$mT, $b_f = 0°$
-110 mT $< B_A < 110$ mT, $B_B > 110$ mT	$B_f = B_A$, $a_f = -0.41°/$mT, $b_f = 90°$
$B_A < -110$ mT, -110 mT $< B_B < 110$ mT	$B_f = B_B$, $a_f = -0.41°/$mT, $b_f = 180°$
-110 mT $< B_A < 110$ mT, $B_B < -110$ mT	$B_f = B_A$, $a_f = 0.41°/$mT, $b_f = 270°$
$B_A > 110$ mT, -110 mT $< B_B < 0$ mT	$B_f = B_B$, $a_f = 0.41°/$mT, $b_f = 360°$

The resolution of the Hall-effect sensor with the 10-bit ADC is 0.39mT at 25°C,

so the resolution of the degree is $0.41°/$mT $\cdot 0.39$ mT $= 0.16°$. This fitting function gives

a linear approach of a sinusoidal behavior, which may have some error in the closed-loop

system with the controller proposed in the next section.

The motor runs below 30 rad/s as tested before. The sampling rate for the sensors

by the Arduino Mega 2560 board in the main loop is closed at 770 Hz, and the controller

with time interrupt is at 100 Hz. In other words, the angular displacement of the motor is

less than 17° in each sampling period. When the motor rotates through the position of 0°,

the position will drop from 360° to 0° or increase from 0° to 360° according to Table 4.1.

The program then calculates the difference between position of two period and compares

it with threshold value of $\pm 90°$ to conclude that the motor rotates counterclockwise or

clockwise at the position of 0°. For example, when $\psi_{k-1} = 5°$ and $\psi_k = 354°$, the

difference value becomes $\psi_k - \psi_{k-1} = 349°$ which is greater than 90°. The program

concludes that the motor just crossed the $0°$ counterclockwise. Then the value of the angular change is $349°-360°= 11°$. Then, we can sense the position at a large scale of range of both positive and negative angles.

4.3. Controller Design

With the dynamic model and all parameter values developed, a PI controller is designed in this section. In Figure 4.7 shows the closed-loop block diagram with $C(s) = K_P + \frac{K_I}{s}$ and $G(s) = \frac{\phi_m}{J_m s^2 + cs}$ according to (4.9). Note in the transfer function of the plant model in the figure, the Coulomb friction is not included in this linear model.
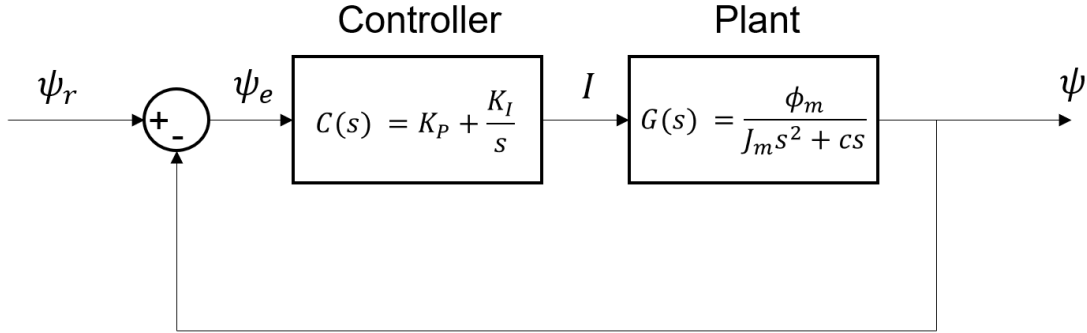
Figure 4.7 Closed-loop diagram of the system.

The closed-loop transfer function of the system in continuous form and the system error $\Psi_e(s)$ are then become (4.15) and (4.16).

$$\frac{\Psi(s)}{\Psi_r(s)} = \frac{G(s)C(s)}{1+G(s)C(s)} = \frac{\phi_m K_P s + \phi_m K_I}{J_m s^3 + cs^2 + \phi_m K_P s + \phi_m K_I} \tag{4.15}$$

$$\Psi_e(s) = \frac{1}{1+G(s)C(s)}\Psi_r(s) = \frac{J_m s^3 + cs^2}{J_m s^3 + cs^2 + \phi_m K_P s + \phi_m K_I}\Psi_r(s) \tag{4.16}$$

Since this is a Type II system [20]. The steady-state error due to a unit step input

is

$$\lim_{t \to +\infty} e(t) * 1(t) = \lim_{s \to 0} s \Psi_e(s) \frac{1}{s} = 0 \tag{4.17}$$

and the steady state error with ramp input is

$$\lim_{t \to +\infty} e(t) * t = \lim_{s \to 0} s \Psi_e(s) \frac{1}{s^2} = 0 \tag{4.18}$$

The transfer function is a third-order system which can be approximated with a second-order dominant. The characteristic polynomial of a second-order dominant system is $(s + \alpha)(s^2 + 2\zeta\omega_n + \omega_n^2)$, where ζ is the closed-loop damping ratio and ω_n is the undamped closed-loop natural frequency. Compared to the denominator in (4.15), the relations between the poles and the control parameters can be derived as

$$\alpha + 2\zeta\omega_n = \frac{c}{J_m} \tag{4.19}$$

$$\omega_n^2 + 2\zeta\omega_n\alpha = \frac{\phi_m K_P}{J_m} \tag{4.20}$$

$$\alpha\omega_n^2 = \frac{\phi_m K_I}{J_m} \tag{4.21}$$

Because the motor has a relatively large Coulomb friction that is not considered as part of the transfer function, the closed-loop system required short rising time of $t_r = 0.12$ s and only a small added damping $\zeta = 0.06$. The nature frequency $\omega_n \cong \frac{1.8}{t_r} = 15$ rad/s. According to section 4.21, $c = 1.23 \times 10^{-3}$ N·m·s and $\phi_m = 1.43 \times 10^{-2}$ Wb. With SolidWorks, $J_m = 5.5 \times 10^{-4}$ kg·m². Then the proportional gain $K_P = \frac{J_m}{\phi}(\omega_n^2 + 2\zeta\omega_n\alpha) \cong 10$ A and the integral gain $K_I = \frac{\alpha\omega_n^2 J_m}{\phi_m} \cong 0.1$ A/s. The digital controller converted with the zero-order hold equivalence is [20]

61

$$C(z) = \frac{I(z)}{\Psi_e(z)} = K_p + \frac{T_s K_I z^{-1}}{1 - z^{-1}} \qquad (4.22)$$

with the sampling period T_s 0.01 s. In the real-time control program, the difference equation for the current input at the kth iteration is

$$i[k] = 10e[k] - 10e[k-1] + i[k-1] \qquad (4.23)$$

where $e[k] = \psi_r - \psi[k]$.

Although the motor can reach 276 rpm with the current input 4.0 A, the power will be cut off in a long time period of test because the inner stator reaches the critical temperature of 80°C. The maximum absolute value of current output is set up as 3 A in simulation of the closed-loop system and actual test. In simulation, we must add the Coulomb friction to the system. From (4.14), we have $J_m \ddot{\psi} + c\dot{\psi} = \phi_m I(t) - K_f \mathrm{sgn}(\dot{\theta}) = \phi_m[I(t) - \frac{K_f}{\phi_m}\mathrm{sgn}(\dot{\theta})]$. To treat the Coulomb friction as a current error in simulation, let $I_f = \frac{K_f}{\phi} = 1.42$ A. A closed-loop control block diagram in Simulink is shown in Figure 4.8.
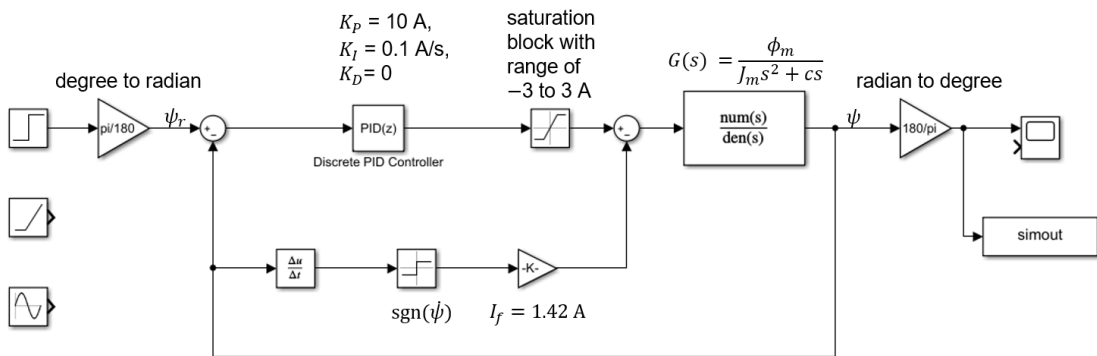
Figure 4.8 The block diagram of closed-loop system in Simulink.

4.4. Experimental Results

From (4.17)–(4.18), the system should track step and ramp position inputs without a steady-state error. The system was tested with step inputs at various positions, various step inputs of motor speed inputs (i.e. position commands with ramp inputs), and sinusoidal position inputs.
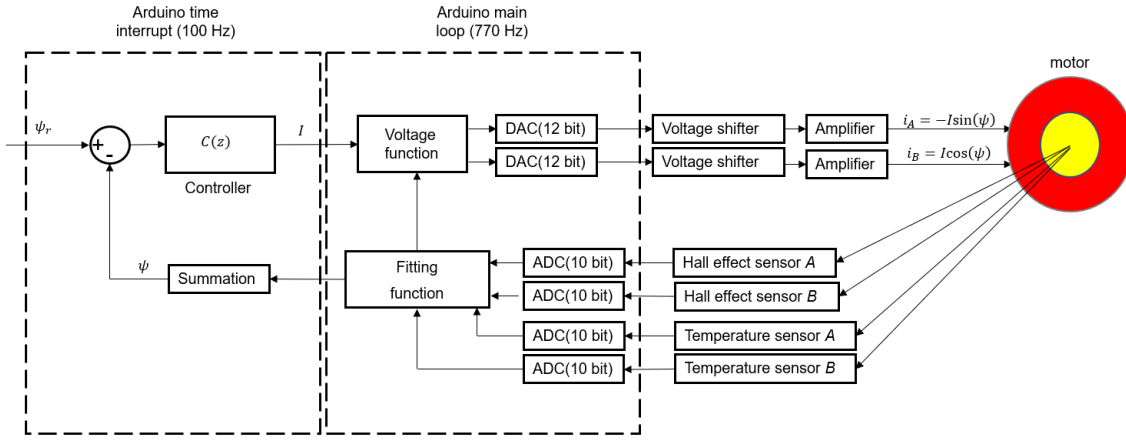
Figure 4.9 Hardware block diagram of HABTPM with the control system.

The experimental results compared with the simulation as in Figure 4.8 are presented to demonstrate the performance of the HABTPM with the control system as shown in Figure 4.9.

In Figure 4.10, the dashed lines show the simulation results by Simulink. In Figure 4.10 (a), the motion of the motor has a significant rising time with some overshoot as predicted in the controller design. There are some transient ridges from the nonlinear behavior caused by fitting function, which has linear approaching to the sinusoidal magnetic flux density change. The final position error is $\pm 0.6°$. Figure 4.10 (b) shows that

the motor tracks the ramp input well in steady state with the speed of 83 rpm. When $t <$ 1.5 s, there is a hunting transient shown in the figure, which is consistent with the simulation result. Figures 4.10 (c) and (d) show that the system can track the sinusoidal reference very well. The HABTPM tracked the motion well within 1.9 s and 3.7 s, respectively. The larger the amplitude is, the longer it takes to reach the steady state. With these results, the HABTPM is proved feasible for precision rotary position-control applications.

The theoretical system resolution is 0.16° given in Section 4.2.2. The controller, however, could not achieve the same resolution due to noise. The repetitive step responses are shown in Figure 4.11. In Figure 4.11 (c), the resolution of the sensing angle with 0.4° is not good enough to be discovered due to high frequency noise. In conclusion, the resolution of the HABTPM with position sensing method and designed controller is proved to be as good as 0.5° resolution shown in Figure 4.11 (b).

(a)

64

(b)

(c)

65
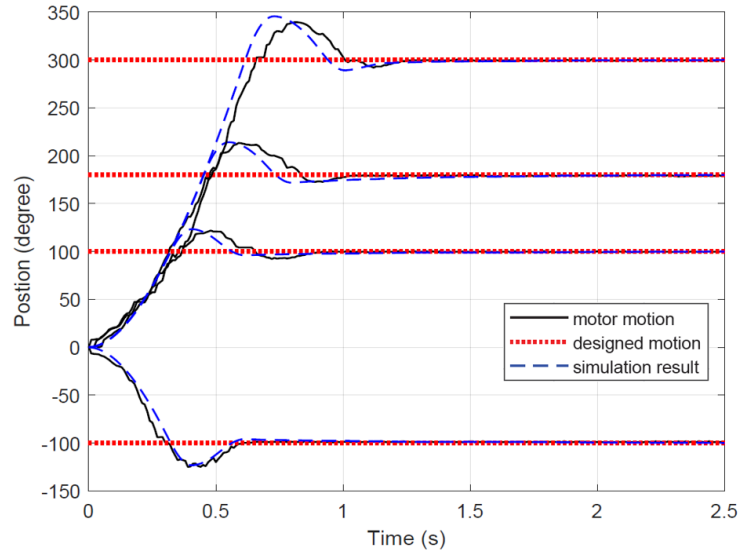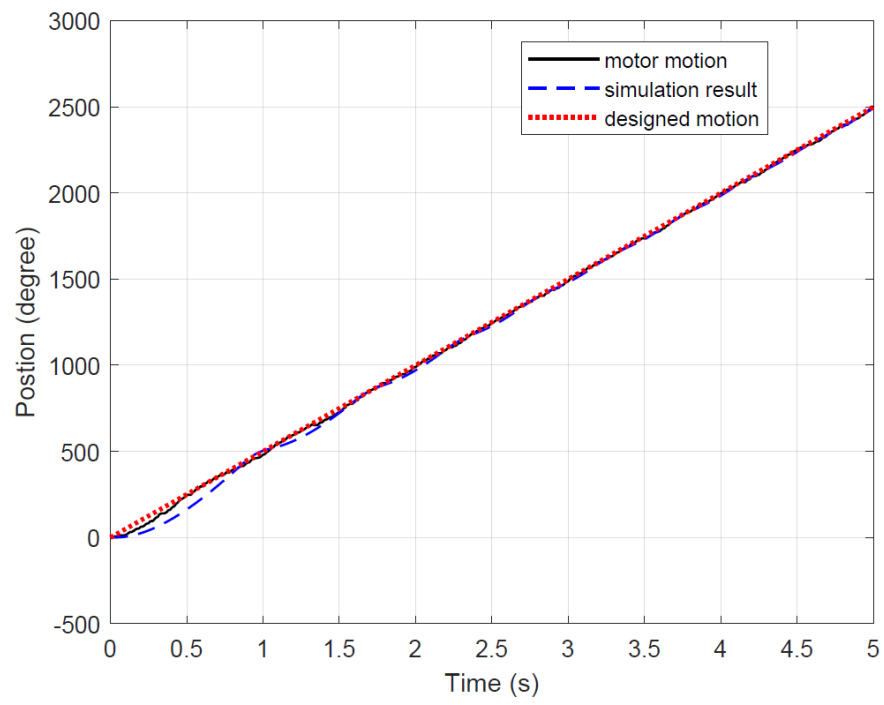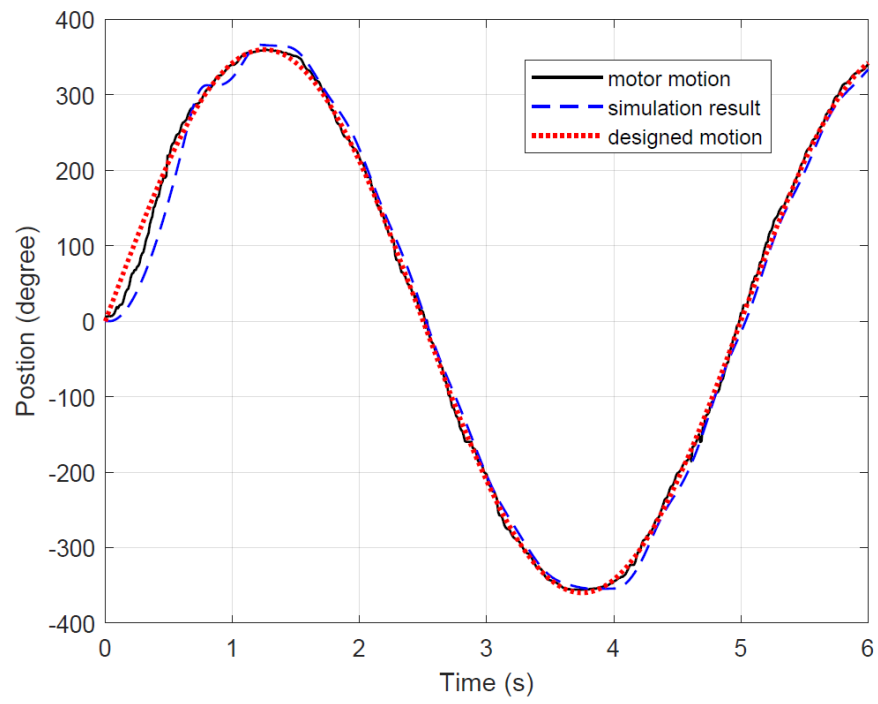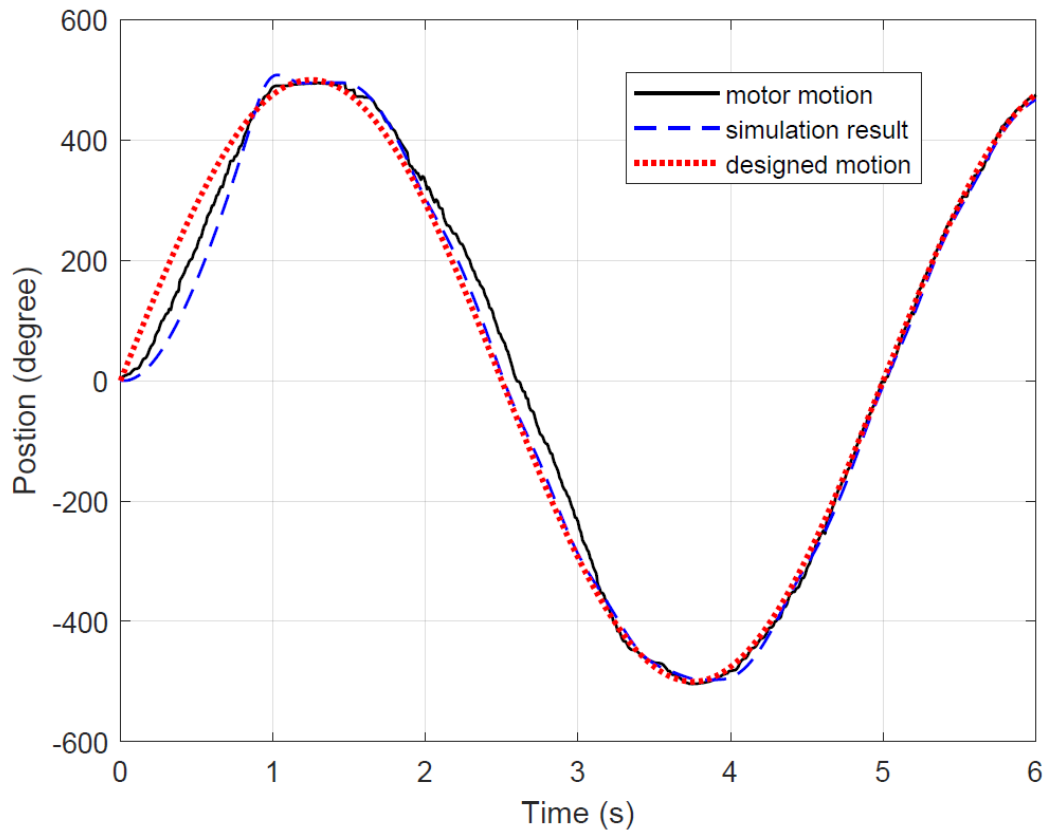
(d)

Figure 4.10 (a) Various step input response ($\pm100°$, 180°, 300°), (b) ramp response (speed at 500°/s), (c) sinusoidal reference response with the magnitude of 360° and the period of 5 s, (d) sinusoidal reference response with the magnitude of 500° and the period of 5 s.

(a)

(b)

67
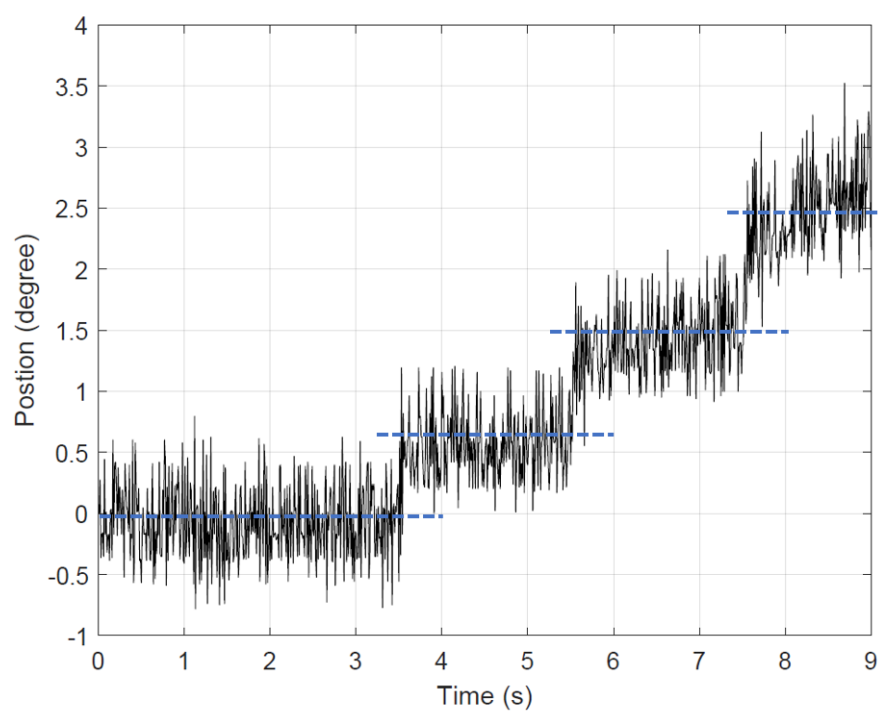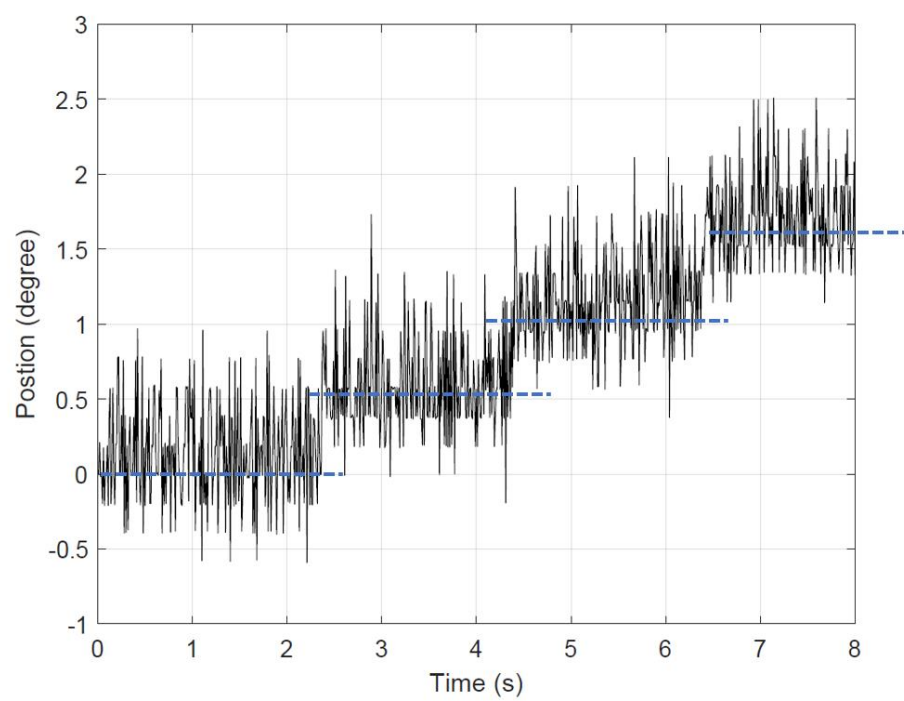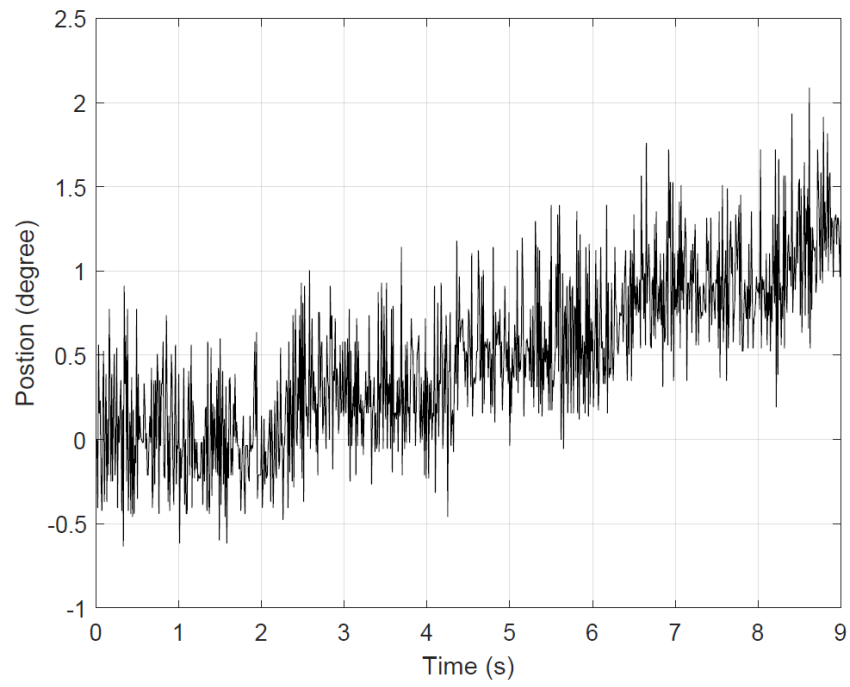
(c)

Figure 4.11 Test results for (a) 0.8°, (b) 0.5°, and (c) 0.4° resolutions test.

5. CONCLUSIONS

5.1. Conclusions

In this thesis, a novel cylindrical Halbach-array-based two-phase motor was proposed and analyzed. A general analysis method, namely the transfer relations of Halbach cylinder was performed to obtain the field solution. The Halbach cylinder in this design can generate a uniform magnetic flux density inside the area of armature. This property simplifies the torque calculation and gives the basis of position with Hall-effect sensors. This theoretical development was verified by an FEA and then the experimental results.

This HABTPM can generate a constant torque with coil currents calculated by volume integration. The theoretical maximum torque generated by the motor at the current input of 4 A is 0.057 N·m. Although the torque that the motor can generate is quite small, the key advantage is that the light-weighted motor with 3D-printed ABS material has no soft iron material, cogging torque, or saliency. Another advantage of the motor is that the dynamics behavior and the controller of the motor are easy to analyze and design. The position of the motor is detected by Hall-effect sensors. With a PI controller designed and implemented in the thesis, the motor has the ability to track the designed motion well with 0.5° resolution.

This thesis provides a design paradigm for new motor design for industrial application. This motor design and position control method can be applied in multiple

engineering fields like wheels of electrical drones, high precision robotic arms, rotation of a radar base, and so on.

5.2. Future Work

There are a lot of improvements can be made in future work. The first thing is the design optimization of the motor volume. With better material other than 3D-printed ABS, the armature inside the cylinder can be enlarged to increase the torque generated by the motor. Another way to increase the torque is to improve the fill factor of the coils. Because of the manual work on the coils, it was only 52.66% in the cross sections of the coils. If the coils were replaced by industrial coils with filling rate of 70%, the rated torque would be increased. Due to the low resolution of 3D-printed material, the alignment of the stator with the ball bearings was not perfect, which caused high Coulomb friction that degraded the performance of the motor. The last improvement would be the replacement of microcontroller with better computing hardware. A faster computer providing a higher sampling rate and an anti-electromagnetic interference data-acquisition card with a higher resolution ADC and DAC will improve the real-time position control performance with a higher resolution.

REFERENCE

[1]   K. Halbach, "Design of permanent multipole magnets with oriented rare earth cobalt material," *Nuclear Instruments and Methods*, vol. 169, no. 1, pp. 1–10, Feb. 1980.

[2]   W.-J. Kim, D. L. Trumper, and J. H. Lang, "Modeling and vector control of planar magnetic levitator," *IEEE Transactions on Industry Applications*, vol. 34, no. 6, pp. 1254–1262, Nov./Dec. 1998.

[3]   T. Hu and W.-J. Kim, "Extended range six-DOF high-precision positioner for wafer processing," *IEEE/ASME Transactions on Mechatronics*, vol. 11, no. 6, pp. 682–689, Dec. 2006.

[4]   V. H. Nguyen and W.-J. Kim, "Two-phase Lorentz coils and linear Halbach array for multiaxis precision-positioning stages with magnetic levitation," *IEEE/ASME Transactions on Mechatronics*, vol. 22, no. 6, pp. 2662–2672, Dec. 2017.

[5]   K. Atallah and D. Howe, "The application of Halbach cylinders to brushless AC servo motors," *IEEE Transactions on Magnetics*, vol. 34, no. 4, pp. 2060–2062, Jul.1998.

[6]   S.-L. Chen, N. Kamaldin, T. J. Teo, W. Liang, C. S. Teo, G. Yang, and K. K. Tan, "Toward comprehensive modeling and large angle tracking control of a limited angle torque actuator with cylindrical Halbach," *IEEE/ASME Transactions on Mechatronics*, vol. 21, no. 1, pp. 431–442, Feb. 2016.

[7]   D. L. Trumper, W.-J. Kim, and M. E. Williams, "Design and analysis framework for linear permanent-magnet machines," *IEEE Transactions on Industry Applications*, vol. 32, no. 2, pp. 371–379, Mar./Apr. 1996.

[8]   V. H. Nguyen and W.-J. Kim, "Novel electromagnetic design for a precision planar positioner moving over a superimposed concentrated-field magnet matrix," *IEEE Transactions on Energy Conversion*, vol. 27, no. 1, pp. 52–62, Mar. 2012.

[9]   A. Insinga, C. Bahl, R. Bjørk, and A. Smith, "Performance of Halbach magnet arrays with finite coercivity," *Journal of Magnetism and Magnetic Materials*, vol. 407, pp. 369–376, Jun. 2016.

[10]   T. Shi, Z. Qiao, C. Xia, H. Li, and Z. Song, "Modeling, analyzing, and parameter design of the magnetic field of a segmented Halbach cylinder," *IEEE Transactions on Magnetics*, vol. 48, no. 5, pp. 1890–1898, May. 2012.

[11]   Z. Q. Zhu, Z. P. Xia, K. Atallah, G. W. Jewell, and D. Howe, "Novel permanent magnet machines using Halbach cylinders," *In Proceedings of the IEEE 3rd Int. Conf. Power Electron. and Motion Control*, pp. 903–908, Aug. 2000.

[12]   Grainger (2020). [Online] Available: https://www.grainger.com/product/NTN-Radial-Ball-Bearing-5U500.

[13]   Texas Instruments, "DRV5055 Ratiometric Linear Hall-Effect Sensor," SBAS640 datasheet, Jan. 2018.

[14]   Analog   Devices   (2020).   [Online]   Available: https://www.analog.com/en/products/tmp36.html?doc=TMP35_36_37.pdf.

[15] Digikey Electronics (2020). [Online] Available: https://www.digikey.com/catalog/en/partgroup/mcp4725-breakout-board/49473.

[16] Digikey Electronics (2020). [Online] Available: https://www.digikey.com/product-detail/en/apex-microtechnology/PA12A/598-1304-ND/.

[17] J. R. Melcher, "Electrodynamic laws, approximations and relations," in *Continuum Electromechanics*, Cambridge, MA, USA: MIT Press, 1981, pp. 2.1–2.54.

[18] Finite Element Method Magnetics. (2019). [Online] Available: http://www.femm.info/

[19] American wire gauge. (2020). [Online] Available: https://en.wikipedia.org/wiki/American_wire_gauge.

[20] G. F. Franklin, J. D. Powell, and A. Emami-Naeini, "Digital Control," in *Feedback Control of Dynamic Systems*, 7th ed., Upper Saddle River, NJ, USA: Prentice Hall, 2015, pp. 590–636.

APPENDIX A

THE C++ CODE FOR ARDUINO MEGA 2560

```
/*  File Name: HABTPMSensor.h
 *  Author: Yuan Wei
 *  Date: November 21, 2019
 *  Description: head files of HABTPMSensor.cpp
 *  Last Changed: N/A
 */


#ifndef HABTPMSENSOR_H
#define HABTPMSENSOR_H


#include <Arduino.h>


class HABTPMSensor
{
  public:
    //default pin numbers for sensors
    uint8_t tempPin = A0;
    uint8_t hallEffectSensorPin = A1;
```

```cpp
    float tempConverter = 500.0 / 1023;

    float BConverter = 5000.0 / 1023;


    //function
    void initializeSensor(uint8_t tempP, uint8_t hallEffectSensorP);

    float getTempt();

    float getB(uint8_t sendRequest);
};


#endif
```

/* File Name: HABTPMSensor.cpp

 * Author: Yuan Wei

 * Date: November 21, 2019

 * Description: get data from temperature sensor and Hall-effect sensor

 * Last Changed: N/A

 */


```cpp
#include "HABTPMSensor.h"


void HABTPMSensor :: initializeSensor(uint8_t tempP, uint8_t hallEffectSensorP)
```

```cpp
{
    tempPin = tempP;

    hallEffectSensorPin = hallEffectSensorP;

    pinMode(tempPin, INPUT);

    pinMode(hallEffectSensorPin, INPUT);

}


float HABTPMSensor :: getTempt()

{
    uint16_t tempV = analogRead(tempPin);

    float temp = float(tempV)*500/1023-50;    //For TMP36 sensor, output Voltage at
25°C (mV) is 750mV, and output Voltage Scaling (mV/°C) is 10mV/°C.

    return temp;

}


float HABTPMSensor :: getB(uint8_t sendRequest)

{
    float B = 0;

    float Sensitivity = 12.5;

    uint16_t data = 0;


    uint16_t tempV = analogRead(tempPin);
```

```
float temp = float(tempV) * tempConverter - 50;


if (temp > 80)

{

    B = 233;        //temperature is too high

}

else

{

    data = analogRead(hallEffectSensorPin);

    Sensitivity = Sensitivity*(1 + 0.0012*(temp - 25));

    B = (data * BConverter - 2500) / Sensitivity;      //mT

}


if (sendRequest == 1)

{

    uint16_t B16 = 0;

    uint8_t BH = 0;

    uint8_t BL = 0;

    B16 = int(B*100);

    BH = B16>>8;

    BL = B16&(0xFF);

    Serial.write(BH);
```

```
    Serial.write(BL);

  }


  return B;

}



/*  File Name: serialSingleWrite.h

 *  Author: Yuan Wei

 *  Date: July 13, 2020

 *  Description: head file of serialSingleWrite

 *  Last Changed: N/A

 */



#ifndef SERIALSINGLEWRITE_H

#define SERIALSINGLEWRITE_H



#include "arduino.h"



void serialSingleWrite(double d);



#endif
```

```cpp
/*  File Name: serialSingleWrite.cpp
 *  Author: Yuan Wei
 *  Date: July 13, 2020
 *  Description: write single(Matlab)/double(Arduino) value to serial
 *  Last Changed: N/A
 */


#include "serialSingleWrite.h"


void serialSingleWrite(double d)
{
 byte * b = (byte *) &d;
 //Serial.print("d:");
 Serial.write(b,4);
 /* DEBUG *
 Serial.println();
 Serial.print(b[0], HEX);
 Serial.print(b[1], HEX);
 Serial.print(b[2], HEX);
 Serial.println(b[3], HEX);*/
```

```
        }



/*  File Name: main.h

 *  Author: Yuan Wei

 *  Date: November 21, 2019

 *  Description: head file of main function

 *  Last Changed: July 17, 2020 by Yuan Wei

 */



#ifndef MAIN_H

#define MAIN_H



#include "arduino.h"

#include "TimerThree.h"

#include "HABTPMSensor.h"

#include "Adafruit_MCP4725.h"

#include "serialSingleWrite.h"



#define Pi 3.14159

#define EI_pin 2

#define timePeriod 10000                        //microseconds
```

```cpp
HABTPMSensor sensorSet1;

HABTPMSensor sensorSet2;

Adafruit_MCP4725 dac1;

Adafruit_MCP4725 dac2;


float getDegree(float B_A, float B_B);

int DACOut(float realVoltage);

float getTheta(float Degree0, float Degree1);

void isrT();

void isrE();


#endif




/*  File Name: main.cpp
 *  Author: Yuan Wei
 *  Date: November 21, 2019
 *  Description: main function of Halbach Array Based Two Phase Motor(HATPM)
 *  Last Changed: August 31, 2020 by Yuan Wei
 */
```

```c
#include "main.h"


unsigned int PhaseAVOut = 2048;

unsigned int PhaseBVOut = 2048;

float Degree0 = 0;

float Degree1 = 0;

float Degree = 0;

double mPosition = 0;

float I = 0;

float Theta_d = 0;

float e0 = 0;

float e1 = 0;

float e2 = 0;

float I0 = 0;

float I1 = 0;

byte ST = 0;

long n = 0;

float resolution = 0.5;


float radianToDegree = 180 / Pi;

float degreeToRadian = Pi / 180;

float voltageConverter = 4095.0 / 1000;
```

```
float speedConverter = 60000000.0 / (360 * timePeriod);          //rpm


void setup()

{

  Serial.begin(115200);

  sensorSet1.initializeSensor(A0, A1);    //tempA A0; HSA A1

  sensorSet2.initializeSensor(A2, A3);    //tempB A2; HSB A3

  dac1.begin(0x62);                //0x62 is the default address of dacMCP4725 with A0
being digital low

  dac2.begin(0x63);                //0x63 is the default address of dacMCP4725 with A0
being digital high

  Timer3.initialize(timePeriod);        // time before overflow in us

  Timer3.attachInterrupt(isrT);        // isrT triggered at overflow

  attachInterrupt(digitalPinToInterrupt(EI_pin), isrE, RISING);

}


void loop()

{

  unsigned long Time = 0;

  float B_A = 0;

  float B_B = 0;

  float temp_A = 0;
```

```cpp
float temp_B = 0;


/*temp_A = sensorSet1.getTempt();

temp_B = sensorSet2.getTempt();*/


//sampling period is 0.4ms

//Time = micros();

B_A = sensorSet1.getB(0);

B_B = sensorSet2.getB(0);

Degree = getDegree(B_A, B_B);


//output

//I = receiveCurrent(receivePin);

//I = 300;

if (Degree > 600)                    //temperature is too high

{

    dac1.setVoltage(2048, false);

    dac2.setVoltage(2048, false);

}

else

{

    PhaseAVOut = DACOut(-I * sin(Degree * degreeToRadian));
```

```
        PhaseBVOut = DACOut(I * cos(Degree * degreeToRadian));

        dac1.setVoltage(PhaseAVOut, false);

        dac2.setVoltage(PhaseBVOut, false);

    }

    //Time = micros() - Time;


    /*Serial.print("T_A:");

    Serial.println(temp_A);

    Serial.print("B_A:");

    Serial.println(B_A);

    Serial.print("T_B:");

    Serial.println(temp_B);

    Serial.print("B_B:");

    Serial.println(B_B);

    Serial.print("Degree:");

    Serial.println(Degree);

    Serial.print("Time:");

    Serial.println(Time);

    Serial.println("------");

    delay(1000);*/


}
```

```
float getDegree(float B_A, float B_B)

{

 float D = 0;


 if(B_A == 233 || B_B == 233)

 {

  D = 666;      //Temperature is too high.

 }

 else if(B_A >= 90)

 {

  D = B_B * 0.5 - 3;

  if(D < 0)

  {

   D = D + 360;

  }

 }

 else if(B_A <= -90)

 {

  D = -B_B * 0.5 + 175.1;

 }

 else if(B_B >= 90)
```

```
  {

    D = -B_A * 0.5 + 85.6;

  }

  else if(B_B <= -90)

  {

    D = B_A * 0.5 + 267.4;

  }


  return D;

}


int DACOut(float realVoltage)

{

    int DACVoltage = int((500 - realVoltage) * voltageConverter);

    return DACVoltage;

}


float getTheta(float Degree0, float Degree1)

{

    float mTheta = 0;

    float D = Degree0 - Degree1;

    if (D > 0)
```

```
{
   if (D < 90)

   {

      mTheta = D;

   }

   else

   {

      mTheta = D - 360;

   }

}

else

{

   if (D > -90)

   {

      mTheta = D;

   }

   else

   {

      mTheta = D + 360;

   }

}

if (abs(D) > 90)
```

```
    {

      mTheta = 0;

    }


    if (abs(mTheta) > 25)

    {

      mTheta = 0;

    }


    return mTheta;

}


void isrT()

{

    //unsigned long Time = 0;

    float mSpeed = 0;

    float If = 0;

    Degree0 = Degree;

    float D = getTheta(Degree0, Degree1);


    if(ST == 1)

    {
```

```
    n++;


    //Theta_d = 5 * n;                        //ramp response

    //Theta_d = 90 * sin(0.4 * Pi * 0.01 * n);       //sine response


    if ( n == 200 || n == 400 || n == 600 || n == 800 || n == 1000)

    {

        Theta_d = Theta_d + resolution;

    }

}


mPosition = mPosition + D;

serialSingleWrite(mPosition);

e0 = (Theta_d - mPosition) * degreeToRadian;

I0 = 10 * e0 - 9.999 * e1 + I1;          //PI

//I0 = 85 * e0 - 78.31 * e1 + 0.6065 * I1;

if (D < 0)

{

    If = -If;

}


if (abs(e0) < 0.17 && abs(e1) < 0.17)
```

```
  {

     If = 0;

  }


  I = I0 * 100 + If;


  /*Saturation Current*/

  if (I > 300)

  {

     I = 300;

  }

  else if (I < -300)

  {

     I = -300;

  }


  Degree1 = Degree0;

  I1 = I0;

  e2 = e1;

  e1 = e0;

  //Time = Time - micros();

}
```

```
void isrE()

{

  if (digitalRead(EI_pin) == 1)

  {

    ST = 1;

    //Theta_d = 1;      //step response

  }

}
```

APPENDIX B

MATLAB CODE

controllerSim.m

```
clc;

clear;


J = 5.5e-4;

c = 2*6.166e-4;

lambda = 2*7.1592e-3;

s = tf('s');

Kp = 10;

Ki = 0.1;

Kd = 0;

Ts = 0.01;

z = 0.001;

p = 10;

K = 0.1;

Td = 1.025e-2;


Cs = Kp+Ki/s+Kd*s;

C2s = (s+z)/(s+p);
```

```
Gs = lambda/(J*s^2+c*s);

figure(1);

% opts = bodeoptions();

% opts.FreqUnits = 'Hz';

margin(Gs);

hold on;

margin(K*Cs*Gs);

grid;

hold off;

figure(2);

rlocus(Cs*Gs);

grid;

ylim([-10, 10]);

C2s = K*C2s;

TFs = minreal(Cs*Gs/(1+Cs*Gs));

figure(3);

step(TFs);

xlim([0 5]);

grid;

Cz = c2d(Cs, Ts, 'zoh')
```

AmpTFSim.m

```matlab
clc;

clear;


R1=10e3;

R2=R1;

R3=R1;

R4=R1;

R5=R1;

R6=27.4e3;

R7=10e3;

R8=R1;

R9=R1;

R10=0.5;

C1=10e-9;

C2=C1;

C3=C1;

Ra=1.5;

La=152e-6;


s = tf('s');

Gs=(R9+R8)*R7*R3*(R6*C3*s+1)/(R1*R5*(R10*(R9+R8)*(R6*C3*s+1)+R9*R7*C3

*(La*s+Ra+R10)*s)*(R3*C2*s+1));
```

```matlab
figure(1);

opts = bodeoptions();

opts.FreqUnits = 'Hz';

bode(Gs,opts);

grid;


figure(2);

step(Gs);

grid;
```

fieldAnalysis.m

```matlab
clc;

clear;


i=1;

d=0.2;

g=2*pi/20-d;

for n=0:70

    Stheta=0;

    S=exp(1i*n*(pi-d/2))-exp(1i*n*(d/2-pi));

    for m=1:19
```

```matlab
    S=S+cos((m-10)*pi/10)*(exp(1i*n*(-pi+d/2+m*(d+g)))-exp(1i*n*(-pi-
d/2+m*(d+g))));

    Stheta=Stheta+sin((m-10)*pi/10)*(exp(1i*n*(-pi+d/2+m*(d+g)))-exp(1i*n*(-pi-
d/2+m*(d+g))));
%        Stheta=Stheta+sin(m*pi/10)*(exp(1i*n*(d/2+2*m*d))-exp(1i*n*(-
d/2+2*m*d)));
    end
    Mr(i,1)=real(-1i*S/(2*pi*n));
    Mri(i,1)=imag(-1i*S/(2*pi*n));
    Mtheta(i,1)=real(-1i*Stheta/(2*pi*n));
    Mthetai(i,1)=imag(-1i*Stheta/(2*pi*n));
        Mx(i,1)=(sin(n*pi/4)+sin(3*n*pi/4)-sin(5*n*pi/4)-sin(7*n*pi/4))/(2*n*pi);
    hn(i,1)=n;
    i=i+1;
end

figure(1);
subplot(2,2,1);
stem(hn,Mr,'k');
xlabel('harmonic number');
ylabel('r-real-magnitude');
ylim([-0.5, 0.5]);
```

```
grid;


subplot(2,2,2);

stem(hn,Mthetai,'k');

xlabel('harmonic number');

ylabel('theta-imaginary-magnitude');

ylim([-0.5, 0.5]);

grid;


subplot(2,2,3);

stem(hn,Mri,'k');

xlabel('harmonic number');

ylabel('r-imaginary-magnitude');

ylim([-0.5, 0.5]);

grid;


subplot(2,2,4);

stem(hn,Mtheta,'k');

xlabel('harmonic number');

ylabel('theta-real-magnitude');

ylim([-0.5, 0.5]);

grid;
```

```
figure(2);

stem(hn,Mx,'k');

xlabel('harmonic number');

ylabel('magnitude');

grid;


Ri=0.031825;

R0=0.038175;

M0=1114084.6*0.3178*2;

Mnt=1114084.6*2*(-0.06353);

Mn=42*Mnt;

n=41;

mu0=pi*4e-7;


f1=(Ri^2+R0^2)/(R0*(Ri^2-R0^2));

f2=(Ri^2+R0^2)/(Ri*(R0^2-Ri^2));

g1=2*Ri/(R0^2-Ri^2);

g2=2*R0/(Ri^2-R0^2);

t1=1+2*Ri^2*(log(Ri)-log(R0))/(R0^2-Ri^2);

t2=1+2*R0^2*(log(Ri)-log(R0))/(R0^2-Ri^2);
```

```
A=[1, -1, 0, 0, 0, 0, 0, 0;

   0, 0, 1, -1, 0, 0, 0, 0;

   1/R0, 0, 0, 0, -1, 0, 0, 0;

   0, -f1, -g1, 0, 0, 1, 0, 0;

   0, -g2, -f2, 0, 0, 0, 1, 0;

   0, 0, 0, 1/Ri, 0, 0, 0, 1;

   0, 0, 0, 0, -1, 1, 0, 0;

   0, 0, 0, 0, 0, 0, -1, 1;];

b=[0; 0; 0; t1; t2; 0; 1; -1]*mu0*M0;

x=A\b
```

```
fn1=n*(Ri^(2*n)+R0^(2*n))/(R0*(Ri^(2*n)-R0^(2*n)));

fn2=n*(Ri^(2*n)+R0^(2*n))/(Ri*(R0^(2*n)-Ri^(2*n)));

gn1=2*n*Ri^n*R0^(n-1)/(R0^(2*n)-Ri^(2*n));

gn2=2*n*Ri^(n-1)*R0^n/(Ri^(2*n)-R0^(2*n));

tn1=(R0*Ri^(2*n) - R0*R0^(2*n) + R0*R0^(2*n)*n + R0*Ri^(2*n)*n -

2*R0^n*Ri*Ri^n*n)/(R0*(n^2 - 1)*(R0^(2*n) - Ri^(2*n)));

tn2=-(R0^(2*n)*Ri - Ri*Ri^(2*n) + R0^(2*n)*Ri*n + Ri*Ri^(2*n)*n -

2*R0*R0^n*Ri^n*n)/(Ri*(n^2 - 1)*(R0^(2*n) - Ri^(2*n)));
```

```
A=[1, -1, 0, 0, 0, 0, 0, 0;
```

```matlab
    0, 0, 1, -1, 0, 0, 0, 0;

    n/R0, 0, 0, 0, -1, 0, 0, 0;

    0, -fn1, -gn1, 0, 0, 1, 0, 0;

    0, -gn2, -fn2, 0, 0, 0, 1, 0;

    0, 0, 0, n/Ri, 0, 0, 0, 1;

    0, 0, 0, 0, -1, 1, 0, 0;

    0, 0, 0, 0, 0, 0, -1, 1;];
b=[0; 0; 0; tn1*Mn; tn2*Mn; 0; Mnt; -Mnt]*mu0;

x=A\b*1000


r = 0.01225;

Br=x(8)*(r/Ri)^(n-1)


% figure(2);

% t=0:0.001:2*pi;

% y=2*0.3178*sin(t)+18*0.1585*sin(19*t)+22*0.1308*sin(21*t)-

38*0.05613*sin(39*t)-42*0.06353*sin(41*t);

% plot(t,y);
```

caluculator.m

```matlab
clc;

clear;
```

```
syms Ri R0 n mu0 M0;

% r = R0;
% f1 = simplify(-n*r^(n-1)/(R0^n-Ri^(2*n)*R0^(-n))-Ri^(2*n)*n*r^(-n-1)/(R0^n-
Ri^(2*n)*R0^(-n)));
% g1 = simplify(n*r^(n-1)*Ri^n*R0^(-n)/(R0^n-Ri^(2*n)*R0^(-n))+Ri^(2*n)*n*r^(-n-
1)*Ri^n*R0^(-n)/(R0^n-Ri^(2*n)*R0^(-n))+Ri^n*n*r^(-n-1));
% t1 = simplify(n*r^(n-1)*(R0-Ri^(n+1)*R0^(-n))/((R0^n-Ri^(2*n)*R0^(-n))*(n^2-
1))+Ri^(2*n)*n*r^(-n-1)*(R0-Ri^(n+1)*R0^(-n))/((R0^n-Ri^(2*n)*R0^(-n))*(n^2-1))-
(Ri^(n+1)*n*r^(-n-1))/(n^2-1)-1/(n^2-1));
%
% r = Ri;
% g2 = simplify(-n*r^(n-1)/(R0^n-Ri^(2*n)*R0^(-n))-Ri^(2*n)*n*r^(-n-1)/(R0^n-
Ri^(2*n)*R0^(-n)));
% f2 = simplify(n*r^(n-1)*Ri^n*R0^(-n)/(R0^n-Ri^(2*n)*R0^(-n))+Ri^(2*n)*n*r^(-n-
1)*Ri^n*R0^(-n)/(R0^n-Ri^(2*n)*R0^(-n))+Ri^n*n*r^(-n-1));
% t2 = simplify(n*r^(n-1)*(R0-Ri^(n+1)*R0^(-n))/((R0^n-Ri^(2*n)*R0^(-n))*(n^2-
1))+Ri^(2*n)*n*r^(-n-1)*(R0-Ri^(n+1)*R0^(-n))/((R0^n-Ri^(2*n)*R0^(-n))*(n^2-1))-
(Ri^(n+1)*n*r^(-n-1))/(n^2-1)-1/(n^2-1));


% f1=(Ri^2+R0^2)/(R0*(Ri^2-R0^2));
```

```matlab
% f2=(Ri^2+R0^2)/(Ri*(R0^2-Ri^2));

% g1=2*Ri/(R0^2-Ri^2);

% g2=2*R0/(Ri^2-R0^2);

% t1=1+2*Ri^2*(log(Ri)-log(R0))/(R0^2-Ri^2);

% t2=1+2*R0^2*(log(Ri)-log(R0))/(R0^2-Ri^2);

%

% A=[1, -1, 0, 0, 0, 0, 0, 0;

%     0, 0, 1, -1, 0, 0, 0, 0;

%     1/R0, 0, 0, 0, -1, 0, 0, 0;

%     0, -f1, -g1, 0, 0, 1, 0, 0;

%     0, -g2, -f2, 0, 0, 0, 1, 0;

%     0, 0, 0, 1/Ri, 0, 0, 0, 1;

%     0, 0, 0, 0, -1, 1, 0, 0;

%     0, 0, 0, 0, 0, 0, -1, 1;];

% b=[0; 0; 0; t1; t2; 0; 1; -1]*mu0*M0;

% x=A\b


fn1=n*(Ri^(2*n)+R0^(2*n))/(R0*(Ri^(2*n)-R0^(2*n)));

fn2=n*(Ri^(2*n)+R0^(2*n))/(Ri*(R0^(2*n)-Ri^(2*n)));

gn1=2*n*Ri^n*R0^(n-1)/(R0^(2*n)-Ri^(2*n));

gn2=2*n*Ri^(n-1)*R0^n/(Ri^(2*n)-R0^(2*n));
```

```
tn1=(R0*Ri^(2*n) - R0*R0^(2*n) + R0*R0^(2*n)*n + R0*Ri^(2*n)*n -

2*R0^n*Ri*Ri^n*n)/(R0*(n^2 - 1)*(R0^(2*n) - Ri^(2*n)));

tn2=-(R0^(2*n)*Ri - Ri*Ri^(2*n) + R0^(2*n)*Ri*n + Ri*Ri^(2*n)*n -

2*R0*R0^n*Ri^n*n)/(Ri*(n^2 - 1)*(R0^(2*n) - Ri^(2*n)));


Mnt = M0;

%Mn = (n+1)*M0;

Mn = (1-n)*M0;


A=[1, -1, 0, 0, 0, 0, 0, 0;

   0, 0, 1, -1, 0, 0, 0, 0;

   n/R0, 0, 0, 0, -1, 0, 0, 0;

   0, -fn1, -gn1, 0, 0, 1, 0, 0;

   0, -gn2, -fn2, 0, 0, 0, 1, 0;

   0, 0, 0, n/Ri, 0, 0, 0, 1;

   0, 0, 0, 0, -1, 1, 0, 0;

   0, 0, 0, 0, 0, 0, -1, 1;];

b=[0; 0; 0; tn1*Mn; tn2*Mn; 0; Mnt; -Mnt]*mu0;

x=A\b
```

FCR.m

```
clc;
```

```matlab
clear;

i=1;

d=0.2;

g=2*pi/20-d;

for n=0:100

    Stheta=0;

    S=-(sin(n*(d/2-pi))-sin(-n*pi)+sin(n*pi)-sin(n*(pi-d/2)));

    for m=1:19

        S=S+cos((m-10)*pi/10)*(sin(n*(-pi+d/2+m*(d+g)))-sin(n*(-pi-d/2+m*(d+g))));

        Stheta=Stheta+sin((m-10)*pi/10)*(cos(n*(-pi+d/2+m*(d+g)))-cos(n*(-pi-d/2+m*(d+g))));

    end

    Mr(i,1)=S/(pi*n);

    Mthetai(i,1)=-Stheta/(pi*n);

    hn(i,1)=n;

    i=i+1;

end

figure(1);

stem(hn,Mr,'k');

xlabel('harmonic number');
```

```matlab
ylabel('r-magnitude');

ylim([-0.4, 0.7]);

grid;


figure(2);

stem(hn,Mthetai,'k');

xlabel('harmonic number');

ylabel('theta-magnitude');

ylim([-0.4, 0.7]);

grid;
```

magnetizationPlot.m
```matlab
clc;

clear;


d = 0.2;

g = pi/10 - d;


figure(1);

hold on;

plot([-pi,-pi+d/2],[-1,-1],'k');

plot([pi-d/2,pi],[-1,-1],'k');
```

```matlab
plot([pi-d/2-g,pi-d/2],[0,0],'k');

for n = 1:1:20

    plot([-pi-d/2+(g+d)*n,-pi+d/2+(g+d)*n],[cos((n-10)*pi/10),cos((n-10)*pi/10)],'k');

    plot([-pi+d/2+(g+d)*(n-1),-pi+d/2+g+(g+d)*(n-1)],[0,0],'k');

    plot([-pi+d/2+(g+d)*(n-1),-pi+d/2+(g+d)*(n-1)],[cos((n-11)*pi/10),0],'k');

    plot([-pi-d/2+(g+d)*n,-pi-d/2+(g+d)*n],[0,cos((n-10)*pi/10)],'k');

end

grid on;

hold off;

xticks([-pi,-pi/2,0,pi/2,pi]);

xticklabels({'-\pi','-\pi/2','0','\pi/2','\pi'});

yticks([-1,-1/2,0,1/2,1]);

yticklabels({'-M_{0}','-M_{0}/2','0','M_{0}/2','M_{0}'});

xlim([-pi, pi]);

ylim([-1.1,1.1]);

xlabel('\theta (rad)');

ylabel('M_{r}');


figure(2);

hold on;

plot([-pi,-pi+d/2],[0,0],'k');

plot([pi-d/2,pi],[0,0],'k');
```

```
for n = 1:1:20

    plot([-pi-d/2+(g+d)*n,-pi+d/2+(g+d)*n],[sin((n-10)*pi/10),sin((n-10)*pi/10)],'k');

    plot([-pi+d/2+(g+d)*(n-1),-pi+d/2+g+(g+d)*(n-1)],[0,0],'k');

    plot([-pi+d/2+(g+d)*(n-1),-pi+d/2+(g+d)*(n-1)],[sin((n-11)*pi/10),0],'k');

    plot([-pi-d/2+(g+d)*n,-pi-d/2+(g+d)*n],[0,sin((n-10)*pi/10)],'k');

end

grid on;

hold off;

xticks([-pi,-pi/2,0,pi/2,pi]);

xticklabels({'-\pi','-\pi/2','0','\pi/2','\pi'});

yticks([-1,-1/2,0,1/2,1]);

yticklabels({'-M_{0}','-M_{0}/2','0','M_{0}/2','M_{0}'});

xlim([-pi, pi]);

ylim([-1.1,1.1]);

xlabel('\theta (rad)');

ylabel('M_{\theta}');
```

dataCollector.slx